Molecular Cell

Article

The ribosome synchronizes folding and assembly to promote oligomeric protein biogenesis

Graphical abstract

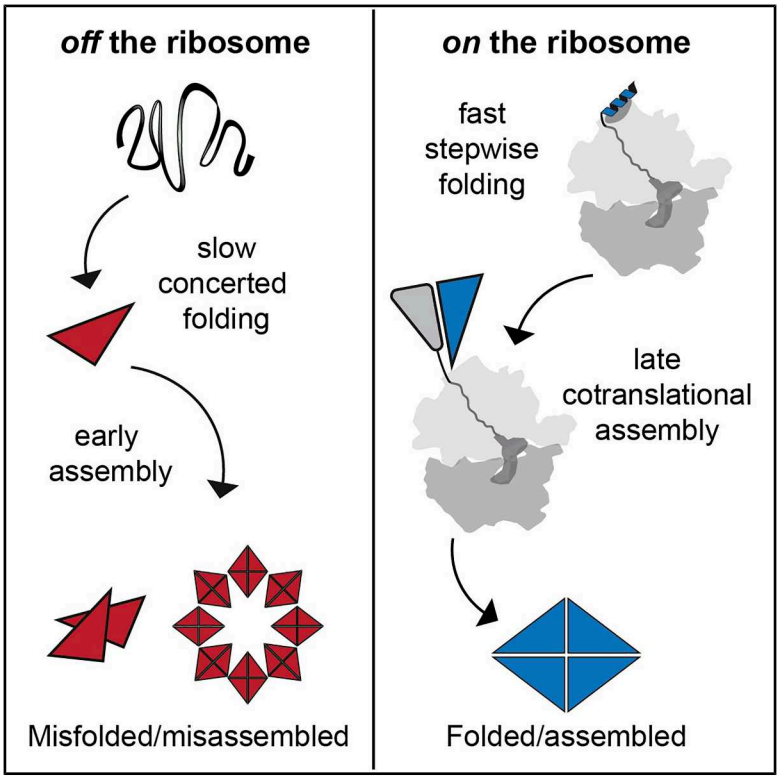

Highlights

- β-gal, a multidomain oligomeric protein, only folds efficiently during translation
- On the ribosome, some domains fold segmentally via small units
- A groove on the ribosome surface binds and stabilizes a nascent amphipathic helix
- β-gal assembly starts during synthesis, avoiding misassembly

Authors

Alžběta Roeselová, Santosh Shivakumaraswamy, Gabija Jurkeviciute, ..., Bernd Bukau, Radoslav I. Enchev, David Balchin

Correspondence

radoslav.enchev@crick.ac.uk (R.I.E.), david.balchin@crick.ac.uk (D.B.)

In brief

Large oligomeric proteins constitute a major fraction of proteomes, but are difficult to refold *in vitro*, raising the question of how cells direct their biogenesis. Roeselová and Shivakumaraswamy et al. show how the ribosome orchestrates efficient cotranslational folding and assembly.

Roeselová et al., 2026, Molecular Cell *86*, 693–706
February 19, 2026
https://doi.org/10.1016/j.molcel.2025.12.022

CellPress

Molecular Cell

CellPress
OPEN ACCESS

Article

The ribosome synchronizes folding and assembly to promote oligomeric protein biogenesis

Alžběta Roeselová,[1,4,8] Santosh Shivakumaraswamy,[1,8] Gabija Jurkeviciute,[2,5] Jessica Zhiyun He,[2,6] Josef Auburger,[3,7] Jaro L. Schmitt,[3] Günter Kramer,[3] Bernd Bukau,[3] Radoslav I. Enchev,[2,*] and David Balchin[1,9,*]

[1]Protein Biogenesis Laboratory, The Francis Crick Institute, London, UK
[2]Visual Biochemistry Laboratory, The Francis Crick Institute, London, UK
[3]Center for Molecular Biology of Heidelberg University (ZMBH), DKFZ-ZMBH Alliance, Heidelberg, Germany
[4]Division of Biosciences, Faculty of Life Science, University College London, London, UK
[5]Department of Neuroscience, Physiology and Pharmacology, University College London, London, UK
[6]Department of Chemistry, Imperial College London, London, UK
[7]Present address: Bayer AG, Research & Development, Pharmaceuticals, 42113 Wuppertal, Germany
[8]These authors contributed equally
[9]Lead contact
*Correspondence: radoslav.enchev@crick.ac.uk (R.I.E.), david.balchin@crick.ac.uk (D.B.)
https://doi.org/10.1016/j.molcel.2025.12.022

SUMMARY

Natural proteins often form intricate multidomain, oligomeric architectures. This presents a prima facie challenge to cellular homeostasis, as topologically complex proteins seldom refold efficiently *in vitro*. Here, we show that the efficient folding and assembly of the five-domain homotetramer β-galactosidase is obligatorily coupled to its synthesis on the ribosome, and we define the underlying mechanisms. During refolding from a denaturant, maturation of the catalytic domain is frustrated. Assembly outpaces monomer folding, and non-native oligomers accumulate. Efficient *de novo* folding is characterized by segmental domain folding, shaped by the binding of a nascent amphipathic helix to a cryptic pocket on uL23 on the ribosome surface. Homomer assembly also initiates cotranslationally via recruitment of a full-length subunit to the nascent polypeptide, and the failure to do so results in misassembly. Our results reveal how the ribosome can dictate the timing of folding and assembly to enable efficient biogenesis of a topologically complex protein.

INTRODUCTION

Small single-domain proteins typically refold rapidly and reversibly *in vitro*, implying that their amino acid sequence suffices to encode productive folding. The "average" protein, however, is large,[1] multidomain,[2] and oligomeric,[3] and refolds slowly or inefficiently in isolation.[4] Based on the relationship between protein length and *in vitro* refolding kinetics, >600 bacterial proteins are predicted to refold slower than the doubling time of *Escherichia coli*.[5] This discrepancy suggests that the cellular environment contributes additional information to folding reactions of topologically complex proteins.

Folding assistance is provided in part by molecular chaperones, which suppress off-pathway aggregation and catalyze refolding following proteotoxic stress.[6,7] In addition, the translating ribosome may direct efficient *de novo* folding during protein synthesis. The ribosome influences protein maturation at different levels. Proximity to the ribosome surface often alters the stability of nascent domains,[8–14] and the vectorial character of protein synthesis can avoid interdomain misfolding.[1,15–17] For oligomeric proteins, assembly frequently initiates on the ribosome.[18–22] Cotranslational assembly can protect unstable subunits from aggregation[21,23] and may contribute to the fidelity of protein complex formation.[24] The ribosome therefore constitutes a unique folding environment, but how exactly this benefits difficult-to-fold proteins is unclear.[25]

Here, we used *E. coli* β-galactosidase (β-gal), a large homotetramer of five-domain subunits,[26] as a model for understanding how the cellular environment optimizes protein folding and assembly (Figure 1A). We show that maturation of β-gal is highly efficient only when folding is coupled to synthesis on the ribosome and use structural and proteomic approaches to provide a molecular rationale. We find that the ribosome directs monomer folding and enforces directional assembly of β-gal subunits. The resulting synchronization between cotranslational folding and assembly avoids kinetic traps that frustrate refolding.

RESULTS

Cotranslational folding enables efficient biogenesis of β-gal

Spontaneous refolding of urea-denatured β-gal *in vitro* was undetectable at 37°C and inefficient (yield < 30%) even at lower temperatures (Figures 1B and S1A). Refolding was also slow,

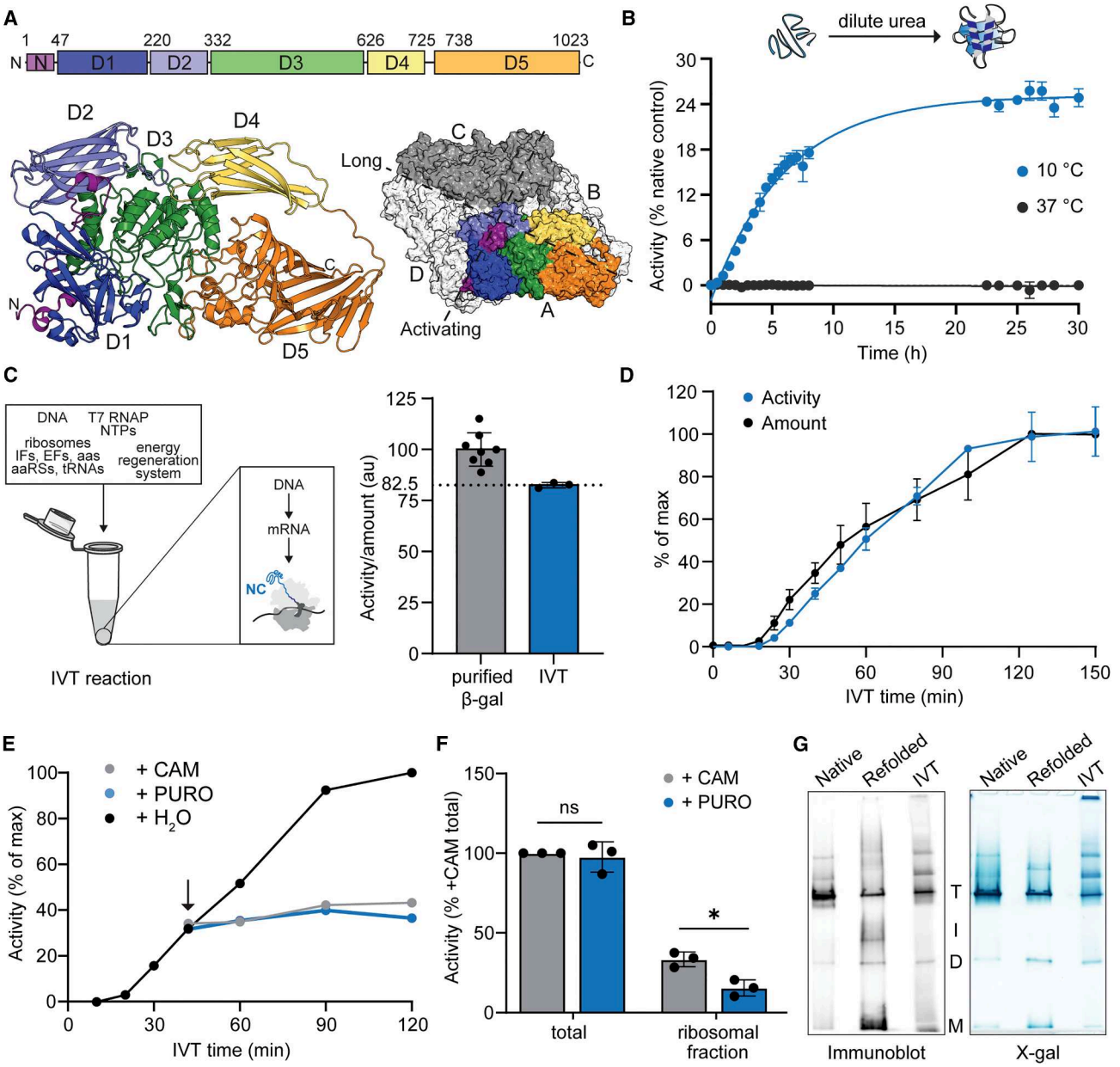

Figure 1. Cotranslational folding enables efficient biogenesis of β-gal

(A) β-gal structure. Top, organization of domains 1–5 (D1–D5). Left, monomer structure (PDB: 6CVM[27]). Right, the tetramer structure is showing long and activating interfaces.

(B) Refolding of β-gal upon dilution from 8 M urea into buffer at 10°C or 37°C, assayed by recovery of enzyme activity. Data were fit to a single exponential function. Yield = 25.1%; 95% confidence interval (CI) 24.5%–25.7%. Half-time = 4.3 h; 95% CI 3.9–4.6 h. Error bars represent SD (n = 3).

(C) Specific activity of β-gal purified from *E. coli* (n = 8 technical replicates) or produced by IVT (n = 3 independent IVT reactions). Data were normalized to the mean specific activity of purified β-gal. Error bars represent SD.

(D) Amount and activity of *in vitro* translated full-length β-gal at different times after initiating IVTs using a plasmid encoding β-gal. Error bars represent SD (n = 3 independent IVT reactions).

(E) Accumulation of β-gal activity during IVT reaction. After 40 min (arrow), reactions were treated with 5 mM chloramphenicol (CAM), 5 mM puromycin (PURO), or an equal volume of water (H_2O).

(F) β-gal activity in the ribosomal fraction of IVTs. β-gal was expressed for 1 h before supplementing the reaction with either CAM to stabilize ribosome-NC complexes or PURO to release NCs. The ribosomal fraction was isolated by sucrose cushion ultracentrifugation. Error bars represent SD (n = 3 independent IVT reactions). ns, $p > 0.05$, $^*p < 0.05$ based on one-way ANOVA with Dunnett's multiple comparisons.

(G) Oligomeric state of natively folded (native), refolded, or IVT-produced β-gal was analyzed using native PAGE. Duplicate gels were immunoblotted for β-gal or stained with the β-gal substrate X-gal. Bands corresponding to the tetramer (T), dimer (D), monomer (M), or intermediate (I) are indicated.

See also Figure S1.

with t½ ~ 4 h at 10°C and ~10 min at 37°C based on extrapolation of the Arrhenius plot (Figures S1A and S1B). The bacterial Hsp70 chaperone system (DnaK, DnaJ, and GrpE) supported only ~20% refolding at 37°C and did not increase the refolding rate (Figure S1C). β-gal refolding is therefore disfavored at physiological temperature and only partially rescued by chaperones.

By contrast, β-gal folded efficiently when produced in a fully reconstituted *in vitro* transcription/translation (IVT) system without chaperones at 37°C, to a yield of 83% ± 1% active protein (Figure 1C). The final yield of β-gal in IVTs was ~1 μM, the same as used in refolding experiments (Figure S1D). Moreover, several observations indicated that *de novo* folding of β-gal is rate-limited by its synthesis on the ribosome. First, the increase in β-gal enzyme activity during ongoing translation was near-concomitant with synthesis of the full-length protein (Figure 1D), consistent with previous work.[28] Second, β-gal activity did not increase after arresting translation using antibiotics (Figure 1E). Third, β-gal activity was detected in the ribosomal fraction of IVT reactions, and this was reduced by the addition of puromycin to release nascent chains (NCs) (Figure 1F). Thus, active β-gal accumulates on translating ribosomes, in agreement with previous *in vivo* observations.[29–32] Together, these data show that cotranslational folding of β-gal, even in the absence of chaperones, is both faster and substantially more efficient than its refolding from denaturant. We next sought to understand the molecular basis for this difference.

Pathway of β-gal refolding from denaturant

We first aimed to understand why β-gal refolds to low yield *in vitro*. The absence of turbidity during refolding suggested that β-gal did not form large aggregates under our experimental conditions, although aggregation could be induced by raising the temperature and lowering the concentration of residual urea (Figure S1E). To account for the fraction of β-gal that failed to refold, we resolved refolding reactions by native PAGE (Figure S1F). Consistent with previous reports,[33,34] tetrameric β-gal accumulated over time at the expense of the monomer and dimer. We also observed a population of β-gal migrating as a diffuse band between dimer and tetramer on native PAGE, which appeared early during refolding and persisted throughout. Prolonged incubation with X-gal revealed enzymatic activity of the monomer and dimer, indicating that they can assemble into active tetramers. However, the intermediate species was inactive (Figures 1G and S1F). Thus, a fraction of β-gal becomes trapped as a non-native oligomer during attempted refolding, limiting the yield of native enzyme. By contrast, IVT-produced β-gal did not contain inactive intermediates (Figure 1G). Cotranslational folding therefore bypasses a misfolding step that leads to off-pathway oligomerization.

The fraction of β-gal that does refold from denaturant refolds slowly. To understand why, we analyzed refolding reactions using hydrogen/deuterium exchange-mass spectrometry (HDX-MS) (Figure 2A). At 16 different times after dilution from denaturant, we pulse-labeled β-gal with D_2O and quantified deuteron incorporation at the peptide level (Figures 2B and 2C). Our HDX-MS experiment followed the on-pathway refolding reaction, since the non-native oligomeric species was depleted during the deuterium labeling step (Figure S1G). We measured refolding kinetics for 400 individual peptides covering 96% of β-gal residues (Figures 2D and S1H; Data S1), allowing us to determine the detailed sequence of refolding events. The data were highly redundant, with each residue reported on by 4.4 peptides on average.

When we mapped peptide folding kinetics onto the native structures of β-gal domains, we noticed that the fast-folding peptides (t½ < 25 min) mapped to central β sheet-rich regions, indicating that the core of each domain folds early and near-simultaneously (Figures 2E and S2A). Fast-folding regions also coincided with the positions of hydrophobic Ile-Leu-Val clusters,[35] suggesting that fast folding is driven by hydrophobic collapse (Figure 2E). Peripheral loops and helices in each domain typically folded more slowly (t½ 25–100 min) than the β sheet cores (Figures 2E and S2A). When we mapped slow refolding peptides (t½ > 100 min), we found that they tended to cluster together in the native structure of β-gal, specifically at domain-domain interfaces involving domain 3 (D3) (Figures 2F, S2B, and S2C). Folding of peptides at domain interfaces also lagged behind those at the long subunit interface, which reached native levels of exchange with t½ < 50 min (Figures S2E and S2F). This implies that dimer assembly initiates before monomer folding completes. Indeed, previous analyses of β-gal refolding kinetics showed that the rate-limiting step is unimolecular and involves maturation of the dimer into a tetramerization-competent state.[33] We found that the slowest event was refolding of residues 3–8, comprising part of the α-peptide at the activating interface, which matched the kinetics of recovery of enzyme activity (Figures 2D and S2D). In summary, slow refolding of β-gal occurs in the following steps (Figure 2G): (1) folding of the β sheet core of each domain, (2) assembly via the long interface, (3) the formation of domain:domain interfaces, (4) the completion of D3 folding, and (5) assembly via the activating interface. Non-native oligomerization is a competitive side reaction, possibly originating from partially folded dimers that accumulate early during refolding.

The ribosome directs segmental folding of the catalytic domain

We next sought to understand how the β-gal monomer folds on the ribosome. To model cotranslational folding intermediates, we prepared a series of 12 stalled ribosome:NC complexes (RNCs), each representing an equilibrium snapshot of biosynthesis[36] (Figures 3A, 3B, S3A, and S3B). Translation was stalled at each domain boundary as well as within individual domains. To remove bound chaperones, we rigorously purified the RNCs from *E. coli* lacking the ribosome-associated chaperone trigger factor. The three longest RNCs were also purified from Δ*lacZ* cells to remove low levels of co-purifying endogenous β-gal (Figure S3B; discussed below).

The analytical complexity of ~2.5 MDa RNCs poses a substantial challenge to probing NC conformation. We used an optimized HDX-MS workflow[8,36] to define the folding status of each NC at the peptide level, using native β-gal as a reference (Figure S3C; Data S2). To uncover regions that fold cooperatively during synthesis, we plotted the uptake of each peptide as a function of NC length and grouped peptides that undergo their final folding transition at the same stage of synthesis (Figures 3C and S4A). We found that peptides grouped by folding behavior also

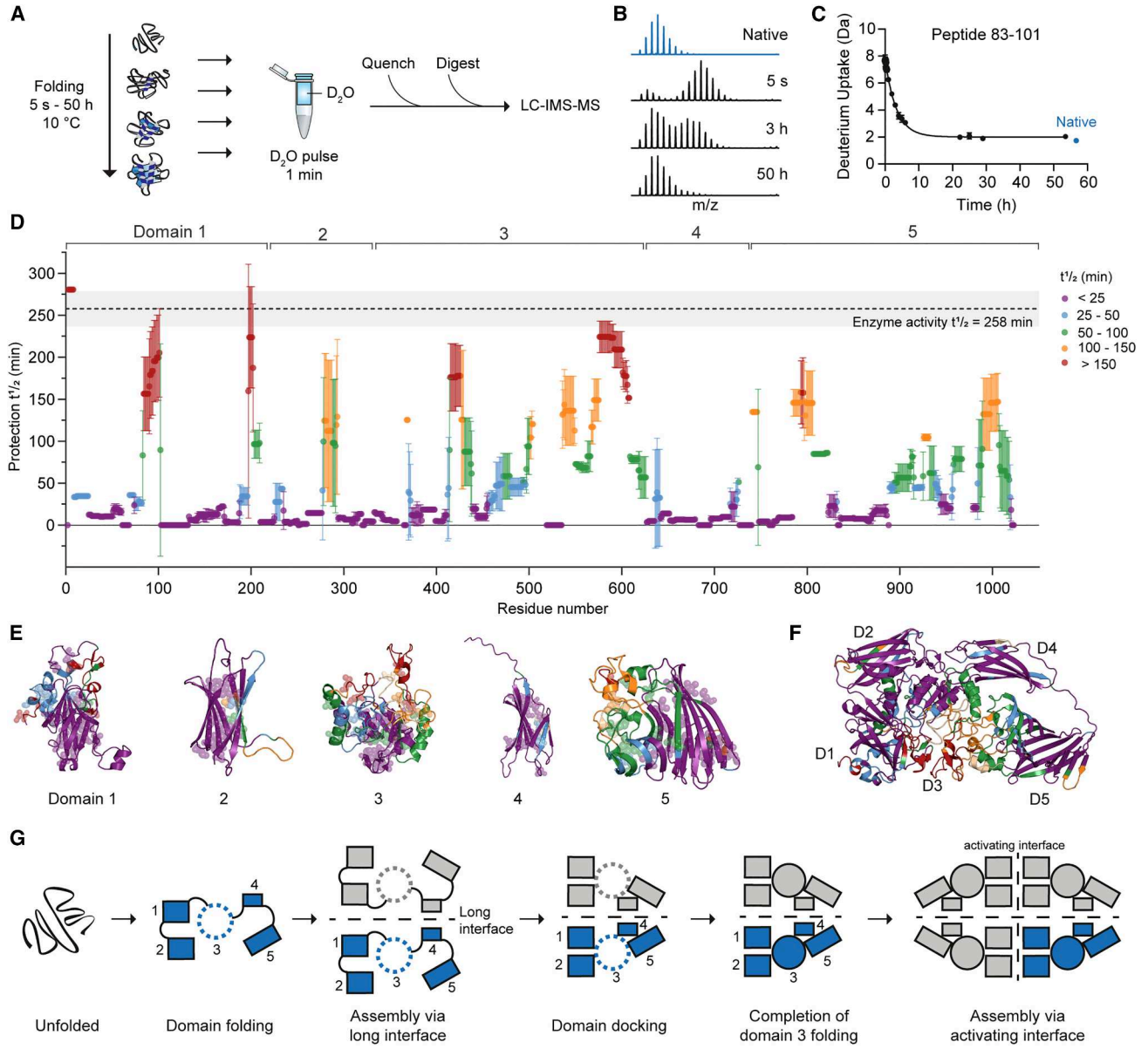

Figure 2. Pathway of β-gal refolding from denaturant

(A) Scheme of HDX-MS experiment.

(B) Representative mass spectra for refolding of peptide 83–101, showing the time-dependent accumulation of the folded (protected) state at the expense of the unfolded (deprotected) state.

(C) Kinetics of peptide 83–101 refolding, calculated from the change in the center of the spectral mass over time. Data were fit to a single exponential function. Error bars represent SD (n = 3).

(D) Half-times of HDX protection for peptides along the sequence of β-gal during refolding. The half-time and 95% CI for recovery of enzyme activity under the same conditions (Figure 1B) are indicated. Error bars represent SD (n = 3).

(E) β-gal domains colored by refolding half-time as in (D). Ile-Leu-Val clusters are shown as semi-transparent spheres.

(F) β-gal subunit colored by refolding half-time as in (D).

(G) Schematic of β-gal refolding pathway.

See also Figure S2 and Data S1.

clustered spatially in the native structure of β-gal, indicating that they behave as cotranslational foldons (Figure 3D). Similar to the refolding reaction, β-rich regions often folded cooperatively on the ribosome. The β sheet cores of D1, D2, and D4 reached near-native levels of deuterium exchange as soon as each complete domain was synthesized, as did a discontinuous β-rich subdomain in D5 (Figure 3D). The core of D1 was folded in $RNC_{1–240}$, D2 in $RNC_{1–352}$, D4 in $RNC_{1–745}$, and a fragment of D5 in

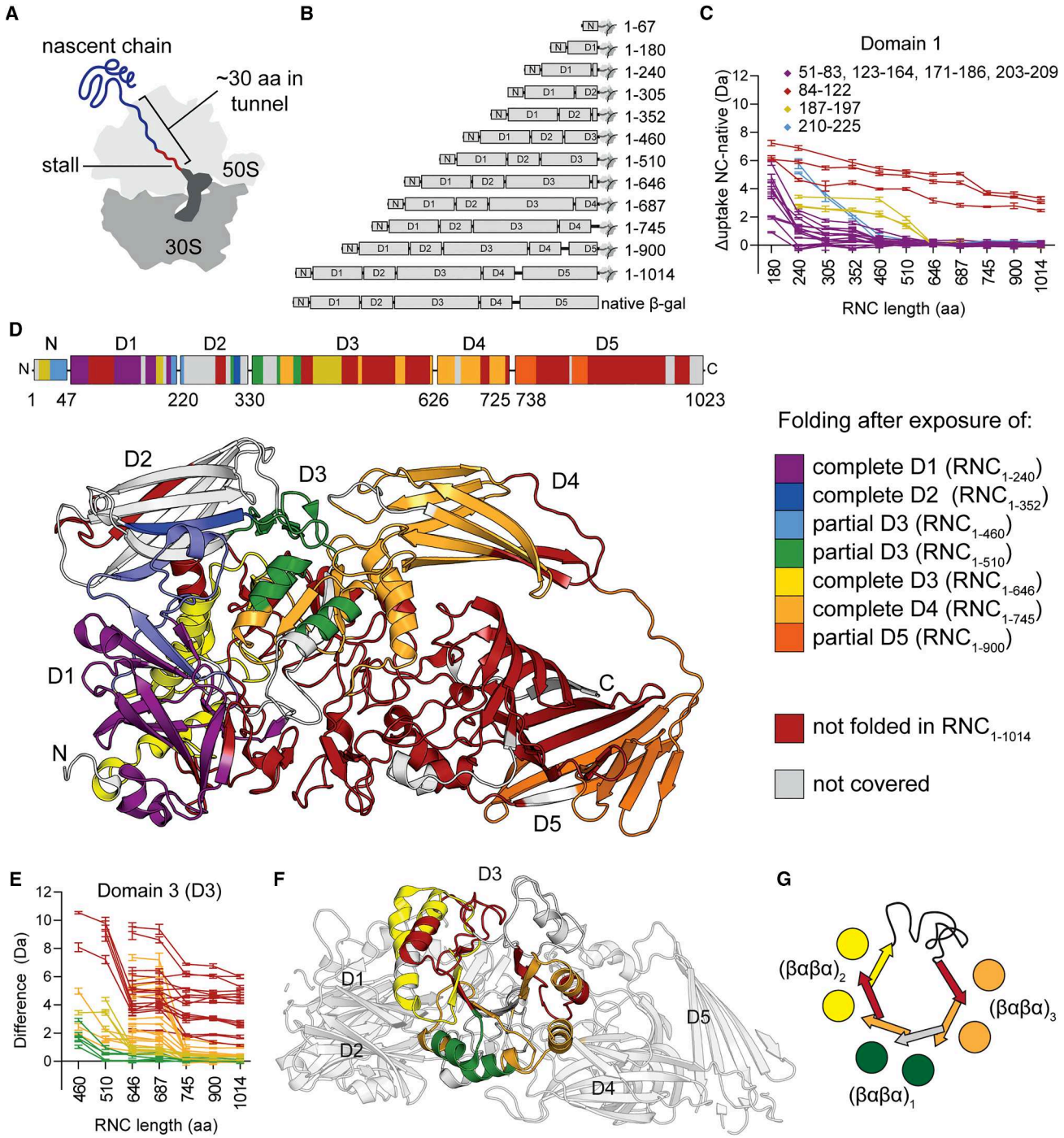

Figure 3. The ribosome directs segmental folding of the β-gal catalytic domain

(A) Schematic of a stalled RNC complex. Synthesis of the stalling sequence (WWWPRIRGPP, red) halts translation and allows isolation of stable RNCs of defined NC length.

(B) Schematic of β-gal RNCs, indicating NC length and domain boundaries.

(C) NC length-dependent protection of D1 peptides from deuterium exchange. The plot shows the difference in deuterium uptake, after 10 s deuteration, between peptides in indicated RNCs and full-length native β-gal. Peptides are grouped according to the NC length at which their level of deuterium uptake plateaus (i.e., changes <1 Da between successive RNCs). Error bars represent SD (n = 3).

(D) Cotranslational foldons. Peptides that plateau at the same NC length are grouped as in (B) and mapped onto the domain schematic (top) and monomer structure (bottom) of β-gal. Peptides that plateau without reaching the same level of uptake as native β-gal, even in the longest RNC, are colored red and designated as "not folded" in $RNC_{1–1,014}$. Regions colored white are not covered by any peptides.

(legend continued on next page)

$RNC_{1–900}$. By contrast, folding of loop- and α-helix-rich regions was often delayed relative to synthesis, suggesting a requirement for long-range stabilizing interactions (Figure 3D). This behavior is exemplified by D1. The central jelly roll of D1 (covered by peptides 51–83, 123–164, 171–186, and 203–209) folded as soon as the domain emerged from the ribosome in $RNC_{1–240}$, while peripheral loops and helices (peptides 187–197 and 210–225) folded upon synthesis of neighboring D2 and D3 (Figures 3C and 3D).

Cotranslational folding of D3 was distinct from other domains (Figures 3E–3G and S4B). D3 houses the active site and resembles a TIM barrel. While typical TIM barrels consist of 4 βαβα repeats and fold into a central β-barrel surrounded by α helices, D3 is distorted and contains only 3 βαβα repeats. Repeat 1 was synthesized in $RNC_{1–460}$ but partially folded only in $RNC_{1–510}$, reflected by decreased deuterium uptake at this NC length. Repeat 2 was synthesized in $RNC_{1–510}$ and partially folded when D3 was complete in $RNC_{1–646}$. Repeat 3 was synthesized in $RNC_{1–646}$ and partially folded when D4 had emerged from the ribosome in $RNC_{1–745}$. Thus, each βαβα repeat begins folding independently, following a short delay relative to their synthesis. Furthermore, the α-helices of each βαβα unit folded at shorter NC lengths than the β strands, indicating that they may fold first during translation. For example, peptides covering α helices in $(βαβα)_1$ reached a native-like level of deuterium uptake in $RNC_{1–510}$, whereas the β strands in the same βαβα unit were folded only in $RNC_{1–745}$ (Figures 3E–3G). The same pattern was apparent for the other two βαβα units. This is in contrast to the refolding reaction, where the core β strands of D3 mature near-simultaneously, followed by peripheral helices (Figure 2E). Together, these data define the sequence of cooperative folding events during β-gal synthesis and reveal segmental, helix-driven folding of the D3 TIM barrel.

The ribosome surface sequesters a nascent amphipathic helix to alter domain folding

The central catalytic domain D3 refolds inefficiently (Figure 2) and populates unique intermediates during efficient folding on the ribosome (Figure 3). To understand how the ribosome modulates folding of this domain, we purified fragments containing the first 2¼ or 2½ domains of β-gal off the ribosome. HDX-MS showed that the 2¼-domain fragment was nearly identical to the corresponding $RNC_{1–460}$, but the 2½-domain NC ($RNC_{1–510}$) was conformationally destabilized on the ribosome as reflected by increased deuterium uptake (Figures 4A and 4B). Destabilized sites were distant from each other in sequence but would cluster together near the C terminus if the NC assumed a near-native tertiary structure (Figure 4C).

To understand the origin of ribosome-induced NC destabilization, we determined the structure of $RNC_{1–510}$ using cryogenic electron microscopy (cryo-EM) (Figures 5A and S5A–S5D). The overall architecture, with the 70S ribosome bound to A- and P-site tRNAs, is similar to previously reported structures of stalled ribosomes.[37] In addition, we observed continuous density for nascent β-gal in the tunnel and against the ribosome surface, of sufficient quality to model both the stalling sequence and the C-terminal 46 residues (465–510) of the β-gal construct (Figure 5B). Residues 485–494 near the vestibule were modeled as an alanine backbone due to limited local resolution. The NC assumes an extended conformation in the exit tunnel and follows a defined path, stabilized by interactions with ribosomal proteins uL4 and uL22 lining the tunnel wall (Figures S6A–S6D). Although it initially follows the contour of uL22, the NC switches trajectory near the vestibule, toward uL29, before emerging from the tunnel close to uL23 (Figures 5A and S6B). Density corresponding to the N-terminal part of the NC (residues 1–464) is visible only at lower contour levels (Figure 5A).

Strikingly, residues 466–478 of β-gal fold into a well-defined α-helix (local resolution 2.8–3.0 Å) outside the vestibule (Figures 5B, 5C, and S5E). The helix is anchored by NC residues Tyr473 and Asn468, which form hydrogen bonds to uL23 residues Met24 and Glu52, respectively. Trp475 of the NC inserts into a pocket formed by Ser34 and Met30 of uL29 and Phe51 of uL23. The groove formed by uL23/uL29 is hydrophobic and accommodates the nonpolar face of the amphipathic NC helix (Figures 5D–5F). Although residues 466–478 are α helical in native β-gal, we found that the equivalent isolated peptide is disordered (Figures S6E and S6F), suggesting that helical structure is stabilized by uL23. Interestingly, the NC-binding pocket we identify is normally occupied by the flexible C terminus of uL23, which is unresolved in our structure and presumably displaced by the NC (Figure 5G). Residues that line the binding pocket and confer its hydrophobic character are evolutionarily conserved (Figure S6G).

Folding of the nascent helix in complex with uL23 explains why $NC_{1–510}$ is locally destabilized on the ribosome. In native β-gal, the hydrophobic face of the helix packs against a hydrophobic groove in D3 (Figure S6H). Interactions with the ribosome therefore compete with intra-NC interactions, disrupting NC folding (Figure 5H). Since the destabilized sites in $RNC_{1–510}$ form part of the same cotranslational foldon (Figures 3C and 4), helix sequestration suffices to destabilize adjacent regions. Importantly, the locally destabilized regions recover when the chain elongates further in $RNC_{1–646}$, indicating that intra-NC interactions eventually outcompete ribosome binding (Figure 4B). In summary, we show that the ribosome surface can modulate domain folding by temporarily sequestering a nascent amphipathic helix in a cryptic hydrophobic pocket. This results in segmental cotranslational maturation of a domain that otherwise refolds in a concerted fashion.

The ribosome directs β-gal assembly to avoid misassembly

During refolding, β-gal assembles prematurely and forms off-pathway oligomers (Figures 1 and 2). By contrast, assembly is efficient when coupled to ongoing translation[39] (Figures 1C–1G). We therefore considered whether the ribosome changes the pathway of β-gal assembly to promote productive folding. Since β-gal is only active when tetrameric, the observation of β-gal activity on

(E) NC length-dependent protection of D3 peptides, as in (B).
(F) Peptide categories mapped onto the structure of the β-gal monomer.
(G) Peptide categories shown schematically.
See also Figures S3 and S4 and Data S2.

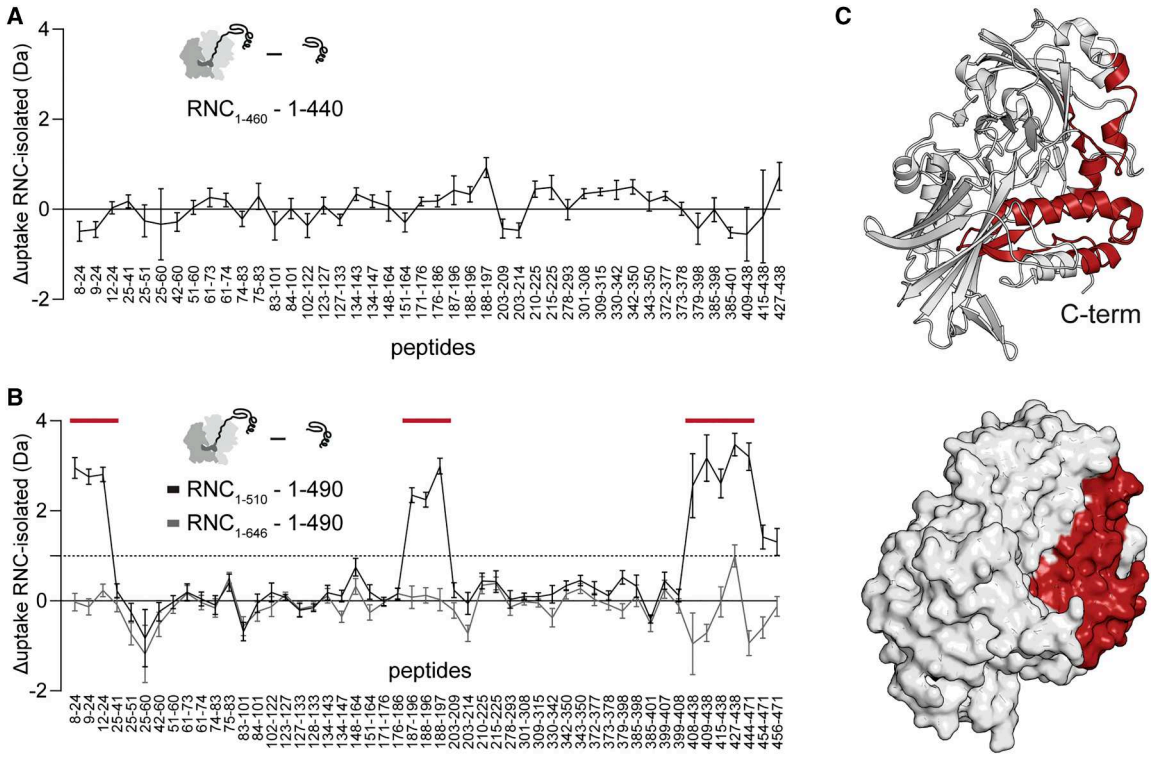

Figure 4. Destabilization of β-gal on the ribosome during D3 synthesis

(A) Effect of the ribosome on β-gal stability. Difference in deuterium uptake, after 100 s deuteration, between truncated β-gal (1–440) and the corresponding $RNC_{1–460}$. Error bars represent SD (n = 3).

(B) As in (A), showing the difference between truncated β-gal (1–490) and $RNC_{1–510}$ or $RNC_{1–646}$. Error bars represent SD (n = 3).

(C) Regions that are deprotected in $RNC_{1–510}$ relative to 1–490 are indicated in red and colored on the native structure of residues 1–490 (PDB: 6CVM[27]).

See also Data S2.

polysomes implies that it assembles to some extent during synthesis (Figure 1F). To probe the underlying mechanism, we first measured enzyme activity of purified β-gal RNCs (Figure 6A). RNCs longer than 745 aa showed low levels of enzyme activity (<5% of $RNC_{FL+50aa}$), indicative of weak or partial assembly. Assembly involved endogenous β-gal, since RNCs produced in Δ*lacZ* cells or IVTs were inactive (Figures 6B and S7A).

Different assembly modes are possible, depending on whether assembly initiates between two incomplete subunits (“co-co” translational) or one incomplete and one complete subunit (“co-post” translational).[21] Consistent with co-post assembly, RNCs longer than 745 aa co-purified with full-length β-gal (Figure S4A). This occurred in wild-type (WT) but not Δ*lacZ* cells and was partially disrupted by mutating the activating interface (Figures S3B and S7B). The co-assembling full-length subunits were protease resistant, suggesting that they are folded (Figure S7C). Thus, mature β-gal subunits assemble with incomplete nascent polypeptides, exposing at minimum the first 4 domains of nascent β-gal.

To test this mechanism *in vivo*, we used selective ribosome profiling (SeRP).[21] Pull-downs using C-terminally tagged β-gal efficiently recovered ribosomes translating *lacZ* mRNA, indicative of co-post assembly (Figure S7D). Analysis of protected footprints revealed that the onset of assembly occurred after synthesis of ~700 aa, stabilized after ~800 aa, and persisted until translation termination, in close agreement with the pull-downs of stalled RNCs (Figure 6C). The late onset of assembly implied that co-post assembly initiates via the long (C-terminal) rather than activating (N-terminal) interface. Consistent with this, a β-gal fragment 1–519, which contains all residues contributing to the activating interface, was monomeric even at a concentration of 900 μM (Figure S7E).

RNCs were inactive when produced *in vitro* in the absence of full-length subunits, arguing against a co-co assembly pathway involving two or more incomplete NCs (Figure S7A). To detect possible co-co assembly *in vivo*, we performed disome selective profiling[20] (Figures S7F and S7G). Co-co assembly is expected to shift translating ribosomes from the monosome to disome fraction after nuclease digestion of the connecting mRNA, resulting in an enrichment of disome footprints at the expense of monosome footprints. No such enrichment was observed for β-gal, indicating that cotranslational β-gal assembly is co-post.

To test whether incomplete chains of β-gal can self-assemble off the ribosome, we purified a 4-domain fragment (1–725), corresponding to the earliest onset of assembly detected by SeRP. We found that 1–725 formed unstable tetramers with weak enzymatic activity (Figures 6D and S9H). However, negative-stain electron microscopy (nsEM) revealed additional higher-order oligomers

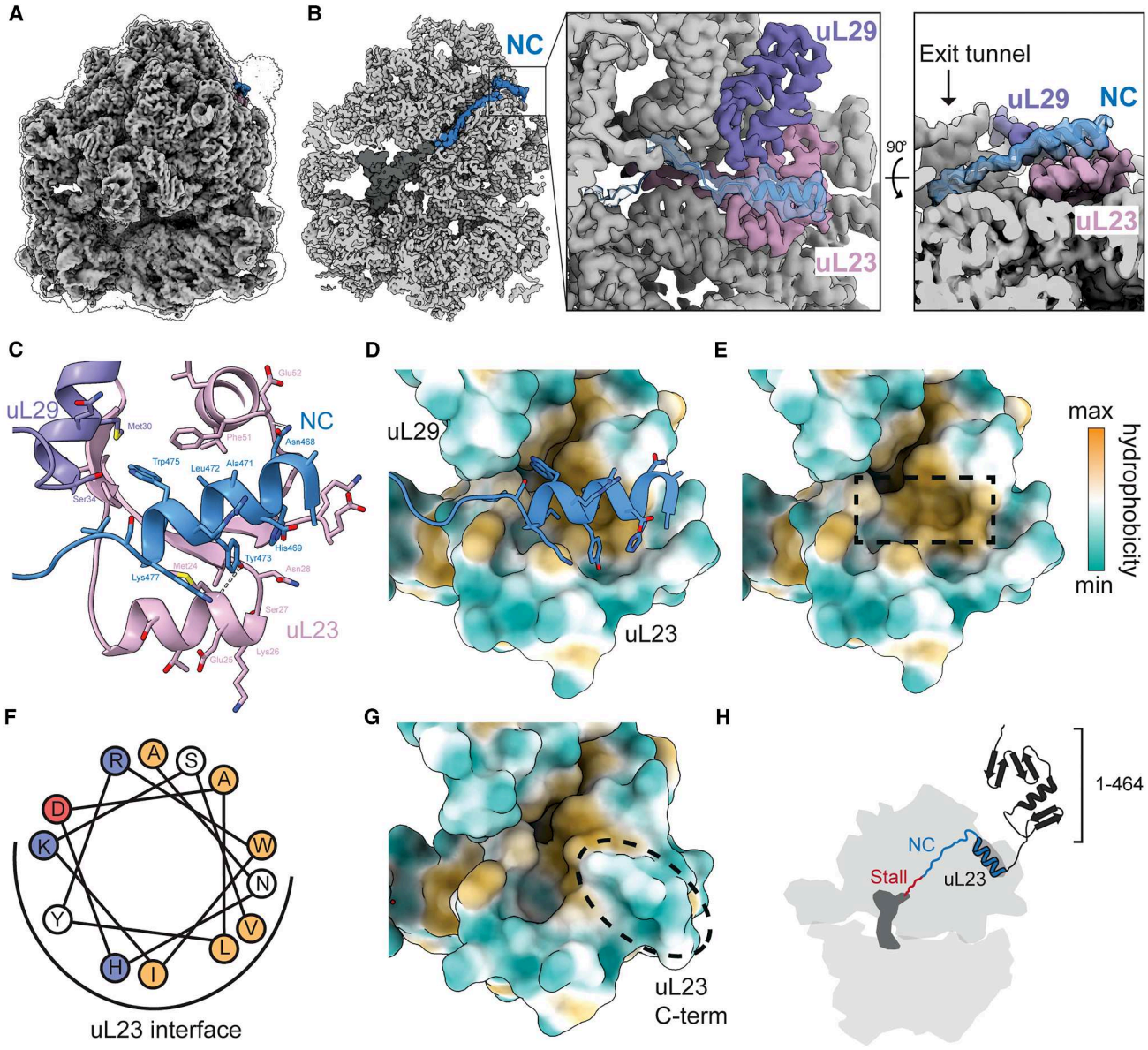

Figure 5. The ribosome surface sequesters a nascent amphipathic helix to alter domain folding

(A) Cryo-EM structure of $RNC_{1–510}$. The silhouette outlines the same map at a lower contour level.

(B) Cross-section of the map, with the peptidyl-tRNA colored dark gray and the NC colored blue. Inset: close-up view of NC interactions with uL23 (salmon) and uL29 (purple). NC density is semi-transparent, and the NC model is shown in cartoon representation.

(C) Interactions between the NC and uL23/uL29.

(D) Model of NC (blue) bound to the ribosome surface, with uL23 and uL29 surfaces colored by hydrophobicity.

(E) As in (D), with the NC removed. The position of the NC helix is indicated by a dashed box.

(F) Helical wheel representation for residues $_{466}$ANHDALYRWIKSV$_{478}$, colored according to electrostatic potential and hydrophobicity (red, negative; blue, positive; orange, hydrophobic).

(G) Surface hydrophobicity of uL23 and uL29 in the 70S ribosome without an NC (7K00[38]). The C terminus of uL23 (residues 89–100) is indicated with a dashed box.

Model for ribosome-induced destabilization of $RNC_{1–510}$. The ribosome sequesters residues 466–478 via a hydrophobic groove on uL23, preventing this region from forming native contacts with the N-terminal part of the NC.

See also Figures S5 and S6 and Table S1.

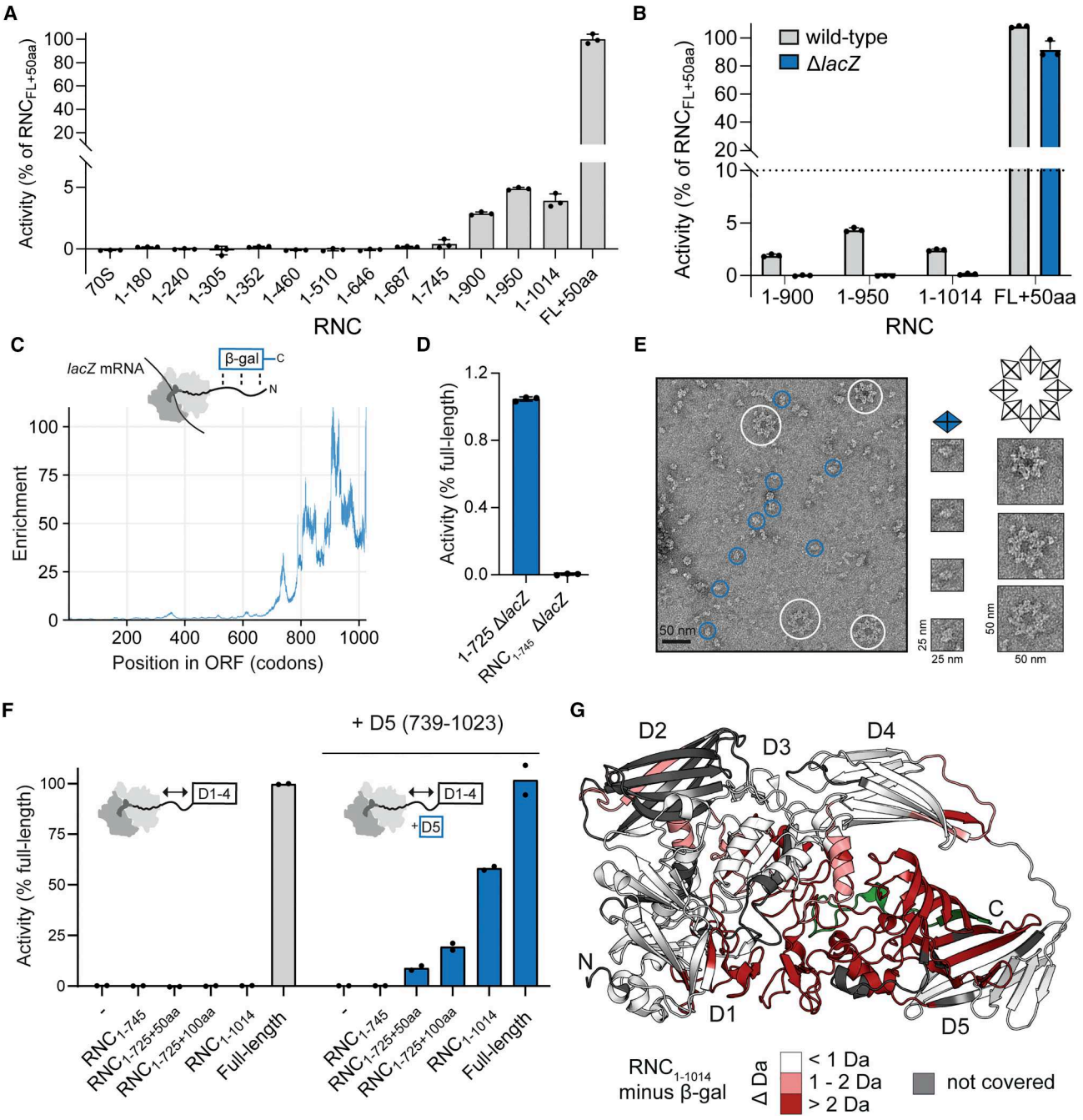

Figure 6. The ribosome directs β-gal assembly to avoid misassembly

(A) β-gal enzyme activity of 5 nM RNCs purified from WT *E. coli*. Error bars represent SD (n = 3).

(B) Endogenous β-gal assembles with RNCs. Enzyme activity of 5 nM RNCs purified from WT or Δ*lacZ E. coli*, which do not express β-gal. Error bars represent SD (n = 3).

(C) Onset of co-post β-gal assembly *in vivo*. SeRP data showing the codon-resolved enrichment (selected translatome/total translatome) of β-gal-bound RNCs along the *lacZ* open reading frame.

(D) D1–D4 are enzymatically active off but not on the ribosome. Enzyme activity of 120 nM 1–725 β-gal truncation (D1–D4) and RNC$_{1–745}$, both purified from Δ*lacZ E. coli*. Error bars represent SD (n = 3).

(E) Truncated β-gal misassembles. Negative-stain EM micrograph of β-gal 1–725 purified from Δ*lacZ E. coli*. Particles corresponding to tetramers or higher-order oligomers are indicated with blue or white circles, respectively.

(legend continued on next page)

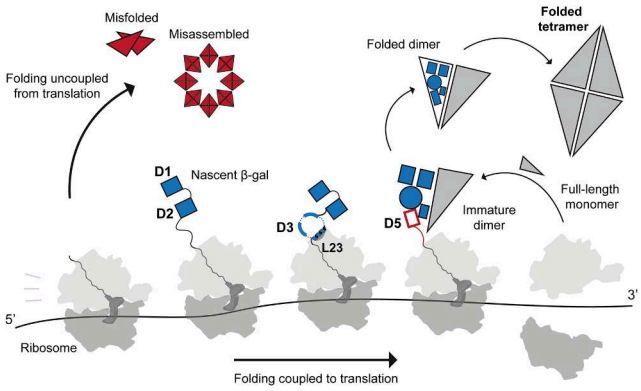

Figure 7. Cotranslational folding and assembly of β-gal

β-gal folds efficiently when coupled to ongoing translation, directed by the ribosome to synchronize with tetramer assembly. D3 folds in discrete steps, the timing of which is dictated by an interaction with a hydrophobic groove on uL23 that stabilizes a nascent amphipathic helix. The pioneering round of translation generates a full-length subunit, which then binds via the long interface to a ribosome-associated subunit during synthesis of D5. An immature dimer results, which matures post translation and assembles via the activating interface to form the folded tetramer. When uncoupled from translation, monomers fold via a less efficient pathway and are prone to misfold and misassemble.

containing 7–8 copies of 1–725 tetramers arranged in a star-like structure (Figures 6E and S7I). Incomplete chains of β-gal are therefore assembly competent off the ribosome but can misassemble. In contrast to isolated 1–725, $RNC_{1–745}$ (purified from Δ*lacZ* cells) was inactive and thus unassembled (Figure 6D). The ribosome therefore inhibits premature co-co assembly, and in doing so prevents misassembly.

To test whether the ribosome sterically interferes with co-co assembly, we purified RNCs exposing residues 1–725 of β-gal fused to C-terminal Gly-Ser linkers of increasing length. These RNCs were inactive but could be activated in a linker length-dependent manner by complementation with folded D5 *in trans* (Figure 6F). Cotranslational assembly is therefore influenced by both subunit folding and proximity to the ribosome.

To understand how folding and assembly are coordinated prior to translation termination, we focused on $RNC_{1–1,014}$. This RNC represents the endpoint of cotranslational maturation, when only ∼30 C-terminal residues remain sequestered in the ribosome exit tunnel. HDX-MS analysis of $RNC_{1–1,014}$ showed that D5 was strongly destabilized compared with native β-gal and must therefore complete folding post translation (Figures 6G and S3C). Since D5 forms the majority of the long interface, post-translational D5 folding may explain why cotranslational assembly strictly requires at least one full-length subunit. Indeed, $RNC_{1–1,014}$ was efficiently activated by purified D5 in *trans*, demonstrating that D5 folding can trigger co-co tetramer assembly on ribosomes (Figure 6F). The ribosome therefore dictates the mode and onset of assembly by controlling the timing of C-terminal domain folding. Assembly is synchronized with monomer folding, rather than preceding folding as occurs during inefficient refolding from denaturant (Figures 2 and S2).

DISCUSSION

By characterizing the maturation of a large multidomain oligomeric protein on and off the ribosome, we uncover new features of cotranslational folding that support the biogenesis of complex folds. We show that the ribosome directs segmental folding of a nascent TIM barrel and uses a conserved hydrophobic groove on uL23 to change the order of folding events such that α-helices fold first (Figure 7). Since isolated secondary structures are intrinsically unstable, nucleating helix folding may promote folding by reducing the entropic barrier.[5,40,41] Indeed, folding of a model protein could be accelerated by stabilizing native-like helical contacts.[42] Our results demonstrate that the ribosome surface is not necessarily generically destabilizing[9,11,43] but can direct specific folding outcomes. Although it is not yet clear whether this phenomenon is general, we note that nascent apomyoglobin was found to dock close to the same hydrophobic pocket on uL23.[44]

Approximately 10% of enzymes contain TIM barrels,[45] and this domain is enriched among substrates of eukaryotic and bacterial chaperonins.[46,47] Interestingly, the segmental, helix-first folding we observe on the ribosome is also characteristic of accelerated TIM barrel folding in the bacterial chaperonin GroEL/ES.[48] Furthermore, GroEL has been shown to stabilize α--helical conformations of bound peptides.[49,50] uL23-directed folding may constitute an alternative, chaperone-independent mechanism supporting TIM barrel biogenesis.

Oligomers present a special biogenesis challenge, as assembly must coordinate with folding while avoiding spurious misassembly.[51–54] Nonetheless, most proteins across all proteomes are oligomeric,[3] implying that oligomer biogenesis is optimized *in vivo*. We find that the ribosome specifies the pathway of β-gal assembly. Although β-gal is a symmetric homomer, cotranslational assembly is directional and involves a full-length and a partially synthesized subunit (Figure 7). This assembly mode may help to confer assembly specificity when multiple oligomeric forms are possible[55,56] (Figure 6E) and avoid misfolding between two incompletely folded subunits[51] (Figure 1G). Since β-gal tetramers are extremely stable,[57,58] the co-assembling full-length subunit is unlikely to originate from mature tetramers *in vivo*. Instead, we propose that the pioneering round of translation generates a subunit which then engages the NC on the trailing ribosome (Figure 7). The polysome may therefore act as a scaffold for efficient co-post homomer assembly. Notably, co-co assembly occurs for only a subset of homomers,

(F) β-gal assembly is triggered by folded D5. Enzyme activity of 7.5 nM β-gal RNCs purified from Δ*lacZ E. coli*, in the absence or presence of isolated folded D5 (residues 739–1,023). The distance between D1 and D4 (residues 1–725) and the ribosome was increased by inserting a 50 or 100 aa Gly-Ser linker between the C terminus of the NC and the stalling sequence. (n = 2)

(G) D5 folds primarily post-translation. Difference in deuterium uptake, after 100 s deuteration, between native β-gal and $RNC_{1–1,014}$ purified from Δ*lacZ E. coli*. Regions that are deprotected in the RNC are colored in shades of red. The C-terminal 30 aa, expected to be inside the exit tunnel in $RNC_{1–1,014}$, are colored green. See also Figure S7.

characterized by intertwined subunits.[18,20,59] Future work will need to establish the prevalence of the alternative co-post homomer assembly mode we describe here.

In summary, we show how the translating ribosome provides a platform for biogenesis of proteins with complex topologies. Together with the chaperone network, this may have shaped the evolution of protein folds by allowing domains and subunits to be combined without compromising foldability.

Limitations of the study

In this study, we used stalled RNCs, purified and stripped of chaperones, as experimentally tractable mimetics of cotranslational folding intermediates. It is not clear to what extent this approach faithfully recapitulates NC conformation during ongoing synthesis in cells.

Although we show that the binding of nascent β-gal to uL23 correlates with specific folding outcomes, it remains to be determined whether this binding is required to influence folding, for β-gal and more generally.

RESOURCE AVAILABILITY

Lead contact

Correspondence and requests for materials should be addressed to David Balchin (david.balchin@crick.ac.uk).

Materials availability

Materials are available from David Balchin upon request under a material transfer agreement with The Francis Crick Institute.

Data and code availability

- The sequencing data discussed in this publication have been deposited in NCBI's Gene Expression Omnibus and are accessible through GEO series accession number GSE291748. Data analysis of ribosome profiling datasets was performed with RiboSeqTools (available at https://github.com/ilia-kats/RiboSeqTools).
- All mass spectrometry data have been deposited to the ProteomeXchange Consortium via the PRIDE partner repository[60] with the following dataset identifiers: HDX-MS analysis of β-gal refolding: PRIDE: PXD063232 and HDX-MS analysis of β-gal truncations and RNCs: PRIDE: PXD060082.
- The cryo-EM map has been deposited in the Electron Microscopy Data Bank (EMDB), and the coordinates have been deposited in the PDB under the following accession numbers: EMDB: EMD-53553 and PDB: 9R3A. Original polyacrylamide gel images and immunoblots have been deposited at Mendeley at Mendeley Data: https://doi.org/10.17632/jssngzcpk6.1 and are publicly available as of the date of publication.
- This paper does not report original code.
- Any additional information required to reanalyze the data reported in this paper is available from the lead contact upon request.

ACKNOWLEDGMENTS

We thank the Francis Crick Institute Proteomics STP (Sarah Maslen and Mark Skehel for help with HDX-MS), the Chemical Biology STP (Dhira Joshi for peptide synthesis, Christelle Soudy for help preparing pepsin beads), the Structural Biology STP (Andrea Nans for cryo-EM data collection, Qu Chen for nsEM training, and Laura Masino for help with circular dichroism), the Scientific Computing STP for support with high-performance computing, Milos Cvetkovic for help with nsEM grid preparation, Stephane Mouilleron for help with SEC-MALS, and all members of the Protein Biogenesis and Visual Biochemistry laboratories for help and discussion. B.B. acknowledges a research grant from the European Union (ERC – SyG – 101072047 – CoTransComplex). Views and opinions expressed are, however, those of the authors only and do not necessarily reflect those of the European Union or the European Research Council. Neither the European Union nor the granting authority can be held responsible for them. J.L.S. was supported by fellowships from the Studienstiftung (German Academic Scholarship Foundation) and the Baden-Württemberg State Graduate Funding (Landesgraduiertenförderung, LGF). J.L.S. is a member of the Heidelberg Biosciences International Graduate School (HBIGS). D.B.'s work is supported by the Francis Crick Institute, which receives its core funding from Cancer Research UK (CC2025), the UK Medical Research Council (CC2025), and the Wellcome Trust (CC2025), and by UK Research and Innovation (UKRI) under the UK Government's Horizon Europe funding guarantee (FoldingMap, EP/X020428/1). Work in the Enchev laboratory is supported by the Francis Crick Institute, with funding from Cancer Research UK (CC2059), the UK Medical Research Council (CC2059), and the Wellcome Trust (CC2059) as well as a Royal Society Wolfson Fellowship and The Crick Chris Banton Translation Fund.

AUTHOR CONTRIBUTIONS

A.R. performed the biochemical and HDX-MS analyses of RNCs. S.S. performed the biochemical and HDX-MS analyses of refolding reactions. G.J. and J.Z.H. collected and analyzed cryo-EM data with help from R.I.E. J.A., J.L.S., G.K., and B.B. performed and analyzed the RiboSeq experiments. D.B. and R.I.E. conceived and supervised the project and wrote the manuscript together with A.R., S.S., G.J., and J.Z.H.

DECLARATION OF INTERESTS

The authors declare no competing interests.

STAR★METHODS

Detailed methods are provided in the online version of this paper and include the following:

- KEY RESOURCES TABLE
- EXPERIMENTAL MODEL AND STUDY PARTICIPANT DETAILS
  - Bacteria strains
- METHOD DETAILS
  - DNA vectors
  - Expression and purification of full-length β-gal
  - RNC buffers
  - Expression and purification of ribosome:nascent chain complexes (RNCs)
  - Expression and purification of β-galactosidase truncations
  - Expression and purification of DnaK, DnaJ and GrpE
  - Size-exclusion chromatography with multi-angle light scattering
  - Immunoblotting
  - β-galactosidase refolding
  - β-galactosidase RNC activity assay
  - In vitro translation
  - Light scattering
  - Native PAGE
  - Limited proteolysis
  - Negative stain EM
  - Cryo-EM sample preparation
  - Cryo-EM data collection and single particle analysis
  - Model building and real-space refinement
  - Circular dichroism spectroscopy
  - Quantification and statistical analysis
  - Pulse-labelled HDX-MS analysis of β-gal refolding
  - Equilibrium HDX-MS analysis of RNCs and β-gal truncations
  - Selective ribosome profiling (SeRP)
  - Disome Selective Profiling (DiSP)
  - Ribosome profiling data analysis

SUPPLEMENTAL INFORMATION

Supplemental information can be found online at https://doi.org/10.1016/j.molcel.2025.12.022.

Received: June 3, 2025
Revised: October 27, 2025
Accepted: December 16, 2025
Published: January 19, 2026

REFERENCES

1. Netzer, W.J., and Hartl, F.U. (1997). Recombination of protein domains facilitated by co-translational folding in eukaryotes. Nature *388*, 343–349. https://doi.org/10.1038/41024.
2. Han, J.-H., Batey, S., Nickson, A.A., Teichmann, S.A., and Clarke, J. (2007). The folding and evolution of multidomain proteins. Nat. Rev. Mol. Cell Biol. *8*, 319–330. https://doi.org/10.1038/nrm2144.
3. Schweke, H., Pacesa, M., Levin, T., Goverde, C.A., Kumar, P., Duhoo, Y., Dornfeld, L.J., Dubreuil, B., Georgeon, S., Ovchinnikov, S., et al. (2024). An atlas of protein homo-oligomerization across domains of life. Cell *187*, 999–1010.e15. https://doi.org/10.1016/j.cell.2024.01.022.
4. Braselmann, E., Chaney, J.L., and Clark, P.L. (2013). Folding the proteome. Trends Biochem. Sci. *38*, 337–344. https://doi.org/10.1016/j.tibs.2013.05.001.
5. Rollins, G.C., and Dill, K.A. (2014). General Mechanism of Two-State Protein Folding Kinetics. J. Am. Chem. Soc. *136*, 11420–11427. https://doi.org/10.1021/ja5049434.
6. Balchin, D., Hayer-Hartl, M., and Hartl, F.U. (2016). In vivo aspects of protein folding and quality control. Science *353*, aac4354. https://doi.org/10.1126/science.aac4354.
7. Balchin, D., Hayer-Hartl, M., and Hartl, F.U. (2020). Recent advances in understanding catalysis of protein folding by molecular chaperones. FEBS Lett. *594*, 2770–2781. https://doi.org/10.1002/1873-3468.13844.
8. Wales, T.E., Pajak, A., Roeselová, A., Shivakumaraswamy, S., Howell, S., Kjær, S., Hartl, F.U., Engen, J.R., and Balchin, D. (2024). Resolving chaperone-assisted protein folding on the ribosome at the peptide level. Nat. Struct. Mol. Biol. *31*, 1888–1897. https://doi.org/10.1038/s41594-024-01355-x.
9. Cabrita, L.D., Cassaignau, A.M.E., Launay, H.M.M., Waudby, C.A., Wlodarski, T., Camilloni, C., Karyadi, M.-E., Robertson, A.L., Wang, X., Wentink, A.S., et al. (2016). A structural ensemble of a ribosome–nascent chain complex during cotranslational protein folding. Nat. Struct. Mol. Biol. *23*, 278–285. https://doi.org/10.1038/nsmb.3182.
10. Streit, J.O., Bukvin, I.V., Chan, S.H.S., Bashir, S., Woodburn, L.F., Włodarski, T., Figueiredo, A.M., Jurkeviciute, G., Sidhu, H.K., Hornby, C.R., et al. (2024). The ribosome lowers the entropic penalty of protein folding. Nature *633*, 232–239. https://doi.org/10.1038/s41586-024-07784-4.
11. Kaiser, C.M., Goldman, D.H., Chodera, J.D., Tinoco, I., and Bustamante, C. (2011). The Ribosome Modulates Nascent Protein Folding. Science *334*, 1723–1727. https://doi.org/10.1126/science.1209740.
12. Chen, X., Rajasekaran, N., Liu, K., and Kaiser, C.M. (2020). Synthesis runs counter to directional folding of a nascent protein domain. Nat. Commun. *11*, 5096. https://doi.org/10.1038/s41467-020-18921-8.
13. Samelson, A.J., Jensen, M.K., Soto, R.A., Cate, J.H.D., and Marqusee, S. (2016). Quantitative determination of ribosome nascent chain stability. Proc. Natl. Acad. Sci. USA *113*, 13402–13407. https://doi.org/10.1073/pnas.1610272113.
14. Agirrezabala, X., Samatova, E., Macher, M., Liutkute, M., Maiti, M., Gil-Carton, D., Novacek, J., Valle, M., and Rodnina, M.V. (2022). A switch from α-helical to β-strand conformation during co-translational protein folding. EMBO J. *41*, e109175. https://doi.org/10.15252/embj.2021109175.
15. Frydman, J., Erdjument-Bromage, H., Tempst, P., and Hartl, F.U. (1999). Co-translational domain folding as the structural basis for the rapid de novo folding of firefly luciferase. Nat. Struct. Biol. *6*, 697–705. https://doi.org/10.1038/10754.
16. Pellowe, G.A., Voisin, T.B., Karpauskaite, L., Maslen, S.L., Roeselová, A., Skehel, J.M., Roustan, C., George, R., Nans, A., Kjær, S., et al. (2024). The human ribosome modulates multidomain protein biogenesis by delaying cotranslational domain docking. Preprint at bioRxiv. https://doi.org/10.1101/2024.09.19.613857.
17. Samelson, A.J., Bolin, E., Costello, S.M., Sharma, A.K., O'Brien, E.P., and Marqusee, S. (2018). Kinetic and structural comparison of a protein's co-translational folding and refolding pathways. Sci. Adv. *4*, eaas9098. https://doi.org/10.1126/sciadv.aas9098.
18. Mallik, S., Venezian, J., Lobov, A., Heidenreich, M., Garcia-Seisdedos, H., Yeates, T.O., Shiber, A., and Levy, E.D. (2024). Structural determinants of co-translational protein complex assembly. Cell *188*, 764–777.e22. https://doi.org/10.1016/j.cell.2024.11.013.
19. Duncan, C.D.S., and Mata, J. (2011). Widespread Cotranslational Formation of Protein Complexes. PLoS Genet. *7*, e1002398. https://doi.org/10.1371/journal.pgen.1002398.
20. Bertolini, M., Fenzl, K., Kats, I., Wruck, F., Tippmann, F., Schmitt, J., Auburger, J.J., Tans, S., Bukau, B., and Kramer, G. (2021). Interactions between nascent proteins translated by adjacent ribosomes drive homomer assembly. Science *371*, 57–64. https://doi.org/10.1126/science.abc7151.
21. Shiber, A., Döring, K., Friedrich, U., Klann, K., Merker, D., Zedan, M., Tippmann, F., Kramer, G., and Bukau, B. (2018). Cotranslational assembly of protein complexes in eukaryotes revealed by ribosome profiling. Nature *561*, 268–272. https://doi.org/10.1038/s41586-018-0462-y.
22. Shieh, Y.-W., Minguez, P., Bork, P., Auburger, J.J., Guilbride, D.L., Kramer, G., and Bukau, B. (2015). Operon structure and cotranslational subunit association direct protein assembly in bacteria. Science *350*, 678–680. https://doi.org/10.1126/science.aac8171.
23. Venezian, J., Bar-Yosef, H., Ben-Arie Zilberman, H., Cohen, N., Kleifeld, O., Fernandez-Recio, J., Glaser, F., and Shiber, A. (2024). Diverging co-translational protein complex assembly pathways are governed by interface energy distribution. Nat. Commun. *15*, 2638. https://doi.org/10.1038/s41467-024-46881-w.
24. Seidel, M., Becker, A., Pereira, F., Landry, J.J.M., de Azevedo, N.T.D., Fusco, C.M., Kaindl, E., Romanov, N., Baumbach, J., Langer, J.D., et al. (2022). Co-translational assembly orchestrates competing biogenesis pathways. Nat. Commun. *13*, 1224. https://doi.org/10.1038/s41467-022-28878-5.
25. Cassaignau, A.M.E., Cabrita, L.D., and Christodoulou, J. (2020). How Does the Ribosome Fold the Proteome? Annu. Rev. Biochem. *89*, 389–415. https://doi.org/10.1146/annurev-biochem-062917-012226.
26. Juers, D.H., Matthews, B.W., and Huber, R.E. (2012). *LacZ* β-galactosidase: Structure and function of an enzyme of historical and molecular biological importance. Protein Sci. *21*, 1792–1807. https://doi.org/10.1002/pro.2165.
27. Bartesaghi, A., Aguerrebere, C., Falconieri, V., Banerjee, S., Earl, L.A., Zhu, X., Grigorieff, N., Milne, J.L.S., Sapiro, G., Wu, X., et al. (2018). Atomic Resolution Cryo-EM Structure of β-Galactosidase. Structure *26*, 848–856.e3. https://doi.org/10.1016/j.str.2018.04.004.
28. Agashe, V.R., Guha, S., Chang, H.-C., Genevaux, P., Hayer-Hartl, M., Stemp, M., Georgopoulos, C., Hartl, F.U., and Barral, J.M. (2004). Function of Trigger Factor and DnaK in Multidomain Protein Folding: Increase in Yield at the Expense of Folding Speed. Cell *117*, 199–209. https://doi.org/10.1016/S0092-8674(04)00299-5.
29. Zipser, D. (1963). Studies on the ribosome-bound β-galactosidase of Escherichia coli. J. Mol. Biol. *7*, 739–751. https://doi.org/10.1016/S0022-2836(63)80120-5.
30. Cowie, D.B., Spiegelman, S., Roberts, R.B., and Duerksen, J.D. (1961). RIBOSOME-BOUND -GALACTOSIDASE. Proc. Natl. Acad. Sci. USA *47*, 114–122. https://doi.org/10.1073/pnas.47.1.114.

31. Hamlin, J., and Zabin, I. (1972). -Galactosidase: Immunological Activity of Ribosome-Bound, Growing Polypeptide Chains. Proc. Natl. Acad. Sci. USA *69*, 412–416. https://doi.org/10.1073/pnas.69.2.412.

32. Dalbow, D.G., and Young, R. (1975). Synthesis Time of beta-Galactosidase in Escherichia coli B/r as a Function of Growth Rate. Biochem. J. *150*, 8.

33. Nichtl, A., Buchner, J., Jaenicke, R., Rudolph, R., and Scheibel, T. (1998). Folding and association of β-galactosidase. J. Mol. Biol. *282*, 1083–1091. https://doi.org/10.1006/jmbi.1998.2075.

34. Freeman, B.C., and Morimoto, R.I. (1996). The human cytosolic molecular chaperones hsp90, hsp70 (hsc70) and hdj-1 have distinct roles in recognition of a non-native protein and protein refolding. EMBO J. *15*, 2969–2979.

35. Kathuria, S.V., Chan, Y.H., Nobrega, R.P., Özen, A., and Matthews, C.R. (2016). Clusters of isoleucine, leucine, and valine side chains define cores of stability in high-energy states of globular proteins: Sequence determinants of structure and stability. Protein Sci. *25*, 662–675. https://doi.org/10.1002/pro.2860.

36. Roeselová, A., Maslen, S.L., Shivakumaraswamy, S., Pellowe, G.A., Howell, S., Joshi, D., Redmond, J., Kjær, S., Skehel, J.M., and Balchin, D. (2024). Mechanism of chaperone coordination during cotranslational protein folding in bacteria. Mol. Cell *84*, 2455–2471.e8. https://doi.org/10.1016/j.molcel.2024.06.002.

37. Gersteuer, F., Morici, M., Gabrielli, S., Fujiwara, K., Safdari, H.A., Paternoga, H., Bock, L.V., Chiba, S., and Wilson, D.N. (2024). The SecM arrest peptide traps a pre-peptide bond formation state of the ribosome. Nat. Commun. *15*, 2431. https://doi.org/10.1038/s41467-024-46762-2.

38. Watson, Z.L., Ward, F.R., Méheust, R., Ad, O., Schepartz, A., Banfield, J.F., and Cate, J.H. (2020). Structure of the bacterial ribosome at 2 Å resolution. eLife *9*, e60482. https://doi.org/10.7554/eLife.60482.

39. Matsuura, T., Hosoda, K., Ichihashi, N., Kazuta, Y., and Yomo, T. (2011). Kinetic Analysis of β-Galactosidase and β-Glucuronidase Tetramerization Coupled with Protein Translation. J. Biol. Chem. *286*, 22028–22034. https://doi.org/10.1074/jbc.M111.240168.

40. Chakrabartty, A., Kortemme, T., and Baldwin, R.L. (1994). Helix propensities of the amino acids measured in alanine-based peptides without helix-stabilizing side-chain interactions. Protein Sci. *3*, 843–852. https://doi.org/10.1002/pro.5560030514.

41. Wright, P.E., Dyson, H.J., and Lerner, R.A. (1988). Conformation of peptide fragments of proteins in aqueous solution: implications for initiation of protein folding. Biochemistry *27*, 7167–7175. https://doi.org/10.1021/bi00419a001.

42. Viguera, A.R., Villegas, V., Avilés, F.X., and Serrano, L. (1997). Favourable native-like helical local interactions can accelerate protein folding. Fold. Des. *2*, 23–33. https://doi.org/10.1016/S1359-0278(97)00003-5.

43. Cassaignau, A.M.E., Włodarski, T., Chan, S.H.S., Woodburn, L.F., Bukvin, I.V., Streit, J.O., Cabrita, L.D., Waudby, C.A., and Christodoulou, J. (2021). Interactions between nascent proteins and the ribosome surface inhibit co-translational folding. Nat. Chem. *13*, 1214–1220. https://doi.org/10.1038/s41557-021-00796-x.

44. Masse, M.M., Hutchinson, R.B., Morgan, C.E., Allaman, H.J., Guan, H., Yu, E.W., and Cavagnero, S. (2024). Mapping Protein–Protein Interactions at Birth: Single-Particle Cryo-EM Analysis of a Ribosome–Nascent Globin Complex. ACS Cent. Sci. *10*, 385–401. https://doi.org/10.1021/acscentsci.3c00777.

45. Nagano, N., Orengo, C.A., and Thornton, J.M. (2002). One Fold with Many Functions: The Evolutionary Relationships between TIM Barrel Families Based on Their Sequences, Structures and Functions. J. Mol. Biol. *321*, 741–765. https://doi.org/10.1016/S0022-2836(02)00649-6.

46. Kerner, M.J., Naylor, D.J., Ishihama, Y., Maier, T., Chang, H.-C., Stines, A.P., Georgopoulos, C., Frishman, D., Hayer-Hartl, M., Mann, M., et al. (2005). Proteome-wide analysis of chaperonin-dependent protein folding in Escherichia coli. Cell *122*, 209–220. https://doi.org/10.1016/j.cell.2005.05.028.

47. Stein, K.C., Kriel, A., and Frydman, J. (2019). Nascent Polypeptide Domain Topology and Elongation Rate Direct the Cotranslational Hierarchy of Hsp70 and TRiC/CCT. Mol. Cell *75*, 1117–1130.e5. https://doi.org/10.1016/j.molcel.2019.06.036.

48. Georgescauld, F., Popova, K., Gupta, A.J., Bracher, A., Engen, J.R., Hayer-Hartl, M., and Hartl, F.U. (2014). GroEL/ES chaperonin modulates the mechanism and accelerates the rate of TIM-barrel domain folding. Cell *157*, 922–934. https://doi.org/10.1016/j.cell.2014.03.038.

49. Landry, S.J., and Gierasch, L.M. (1991). The chaperonin GroEL binds a polypeptide in an alpha-helical conformation. Biochemistry *30*, 7359–7362. https://doi.org/10.1021/bi00244a001.

50. Landry, S.J., Jordan, R., McMacken, R., and Gierasch, L.M. (1992). Different conformations for the same polypeptide bound to chaperones DnaK and GroEL. Nature *355*, 455–457. https://doi.org/10.1038/355455a0.

51. Natan, E., Endoh, T., Haim-Vilmovsky, L., Flock, T., Chalancon, G., Hopper, J.T.S., Kintses, B., Horvath, P., Daruka, L., Fekete, G., et al. (2018). Cotranslational protein assembly imposes evolutionary constraints on homomeric proteins. Nat. Struct. Mol. Biol. *25*, 279–288. https://doi.org/10.1038/s41594-018-0029-5.

52. Natan, E., Wells, J.N., Teichmann, S.A., and Marsh, J.A. (2017). Regulation, evolution and consequences of cotranslational protein complex assembly. Curr. Opin. Struct. Biol. *42*, 90–97. https://doi.org/10.1016/j.sbi.2016.11.023.

53. Jaenicke, R., and Seckler, R. (1997). Protein Misassembly *IN VITRO*. In Advances in Protein Chemistry Protein Misassembly-C10, F.M. Richards, D.S. Eisenberg, and P.S. Kim, eds. (Academic Press), pp. 1–59. https://doi.org/10.1016/S0065-3233(08)60318-6.

54. Schwarz, A., and Beck, M. (2019). The Benefits of Cotranslational Assembly: A Structural Perspective. Trends Cell Biol. *29*, 791–803. https://doi.org/10.1016/j.tcb.2019.07.006.

55. Sendker, F.L., Schlotthauer, T., Mais, C.-N., Lo, Y.K., Girbig, M., Bohn, S., Heimerl, T., Schindler, D., Weinstein, A., Metzger, B.P.H., et al. (2024). Frequent transitions in self-assembly across the evolution of a central metabolic enzyme. Nat. Commun. *15*, 10515. https://doi.org/10.1038/s41467-024-54408-6.

56. Sendker, F.L., Lo, Y.K., Heimerl, T., Bohn, S., Persson, L.J., Mais, C.-N., Sadowska, W., Paczia, N., Nußbaum, E., del Carmen Sánchez Olmos, M., et al. (2024). Emergence of fractal geometries in the evolution of a metabolic enzyme. Nature *628*, 894–900. https://doi.org/10.1038/s41586-024-07287-2.

57. Li, X., Jiang, Y., Chong, S., and Walt, D.R. (2018). Bottom-up single-molecule strategy for understanding subunit function of tetrameric β--galactosidase. Proc. Natl. Acad. Sci. USA *115*, 8346–8351. https://doi.org/10.1073/pnas.1805690115.

58. Mogalisetti, P., and Walt, D.R. (2015). Stoichiometry of the α--Complementation Reaction of Escherichia coli β-Galactosidase As Revealed through Single-Molecule Studies. Biochemistry *54*, 1583–1588. https://doi.org/10.1021/bi5015024.

59. Badonyi, M., and Marsh, J.A. (2022). Large protein complex interfaces have evolved to promote cotranslational assembly. eLife *11*, e79602. https://doi.org/10.7554/eLife.79602.

60. Perez-Riverol, Y., Bai, J., Bandla, C., García-Seisdedos, D., Hewapathirana, S., Kamatchinathan, S., Kundu, D.J., Prakash, A., Frericks-Zipper, A., Eisenacher, M., et al. (2022). The PRIDE database resources in 2022: a hub for mass spectrometry-based proteomics evidences. Nucleic Acids Res. *50*, D543–D552. https://doi.org/10.1093/nar/gkab1038.

61. Cymer, F., Hedman, R., Ismail, N., and von Heijne, G. (2015). Exploration of the Arrest Peptide Sequence Space Reveals Arrest-enhanced Variants. J. Biol. Chem. *290*, 10208–10215. https://doi.org/10.1074/jbc.M115.641555.

62. Studier, F.W. (2005). Protein production by auto-induction in high-density shaking cultures. Protein Expr. Purif. *41*, 207–234. https://doi.org/10.1016/j.pep.2005.01.016.

63. Didovyk, A., Tonooka, T., Tsimring, L., and Hasty, J. (2017). Rapid and Scalable Preparation of Bacterial Lysates for Cell-Free Gene Expression. ACS Synth. Biol. *6*, 2198–2208. https://doi.org/10.1021/acssynbio.7b00253.

64. Hansen, S., Stüber, J.C., Ernst, P., Koch, A., Bojar, D., Batyuk, A., and Plückthun, A. (2017). Design and applications of a clamp for Green Fluorescent Protein with picomolar affinity. Sci. Rep. *7*, 16292. https://doi.org/10.1038/s41598-017-15711-z.

65. Gasteiger, E., Hoogland, C., Gattiker, A., Duvaud, S., Wilkins, M.R., Appel, R.D., and Bairoch, A. (2005). Protein Identification and Analysis Tools on the ExPASy Server. In The Proteomics Protocols Handbook, J.M. Walker, ed. (Humana Press), pp. 571–607. https://doi.org/10.1385/1-59259-890-0:571.

66. Schindelin, J., Arganda-Carreras, I., Frise, E., Kaynig, V., Longair, M., Pietzsch, T., Preibisch, S., Rueden, C., Saalfeld, S., Schmid, B., et al. (2012). Fiji: an open-source platform for biological-image analysis. Nat. Methods *9*, 676–682. https://doi.org/10.1038/nmeth.2019.

67. Scheres, S.H.W. (2012). RELION: Implementation of a Bayesian approach to cryo-EM structure determination. J. Struct. Biol. *180*, 519–530. https://doi.org/10.1016/j.jsb.2012.09.006.

68. Rohou, A., and Grigorieff, N. (2015). CTFFIND4: Fast and accurate defocus estimation from electron micrographs. J. Struct. Biol. *192*, 216–221. https://doi.org/10.1016/j.jsb.2015.08.008.

69. Bepler, T., Morin, A., Rapp, M., Brasch, J., Shapiro, L., Noble, A.J., and Berger, B. (2019). Positive-unlabeled convolutional neural networks for particle picking in cryo-electron micrographs. Nat. Methods *16*, 1153–1160. https://doi.org/10.1038/s41592-019-0575-8.

70. Punjani, A., Rubinstein, J.L., Fleet, D.J., and Brubaker, M.A. (2017). cryoSPARC: algorithms for rapid unsupervised cryo-EM structure determination. Nat. Methods *14*, 290–296. https://doi.org/10.1038/nmeth.4169.

71. Punjani, A., and Fleet, D.J. (2021). 3D variability analysis: Resolving continuous flexibility and discrete heterogeneity from single particle cryo-EM. J. Struct. Biol. *213*, 107702. https://doi.org/10.1016/j.jsb.2021.107702.

72. Punjani, A., Zhang, H., and Fleet, D.J. (2020). Non-uniform refinement: adaptive regularization improves single-particle cryo-EM reconstruction. Nat. Methods *17*, 1214–1221. https://doi.org/10.1038/s41592-020-00990-8.

73. Pettersen, E.F., Goddard, T.D., Huang, C.C., Meng, E.C., Couch, G.S., Croll, T.I., Morris, J.H., and Ferrin, T.E. (2021). UCSF ChimeraX: Structure visualization for researchers, educators, and developers. Protein Sci. *30*, 70–82. https://doi.org/10.1002/pro.3943.

74. Croll, T.I. (2018). ISOLDE: a physically realistic environment for model building into low-resolution electron-density maps. Acta Crystallogr. D Struct. Biol. *74*, 519–530. https://doi.org/10.1107/S2059798318002425.

75. Liebschner, D., Afonine, P.V., Baker, M.L., Bunkóczi, G., Chen, V.B., Croll, T.I., Hintze, B., Hung, L.W., Jain, S., McCoy, A.J., et al. (2019). Macromolecular structure determination using X-rays, neutrons and electrons: recent developments in Phenix. Acta Crystallogr. D Struct. Biol. *75*, 861–877. https://doi.org/10.1107/S2059798319011471.

76. Davis, I.W., Leaver-Fay, A., Chen, V.B., Block, J.N., Kapral, G.J., Wang, X., Murray, L.W., Arendall, W.B., Snoeyink, J., Richardson, J.S., et al. (2007). MolProbity: all-atom contacts and structure validation for proteins and nucleic acids. Nucleic Acids Res. *35*, W375–W383. https://doi.org/10.1093/nar/gkm216.

77. Sreerama, N., and Woody, R.W. (2000). Estimation of protein secondary structure from circular dichroism spectra: comparison of CONTIN, SELCON, and CDSSTR methods with an expanded reference set. Anal. Biochem. *287*, 252–260. https://doi.org/10.1006/abio.2000.4880.

78. Ferruz, N., Schmidt, S., and Höcker, B. (2021). ProteinTools: a toolkit to analyze protein structures. Nucleic Acids Res. *49*, W559–W566. https://doi.org/10.1093/nar/gkab375.

79. Krissinel, E., and Henrick, K. (2007). Inference of Macromolecular Assemblies from Crystalline State. J. Mol. Biol. *372*, 774–797. https://doi.org/10.1016/j.jmb.2007.05.022.

80. Masson, G.R., Burke, J.E., Ahn, N.G., Anand, G.S., Borchers, C., Brier, S., Bou-Assaf, G.M., Engen, J.R., Englander, S.W., Faber, J., et al. (2019). Recommendations for performing, interpreting and reporting hydrogen deuterium exchange mass spectrometry (HDX-MS) experiments. Nat. Methods *16*, 595–602. https://doi.org/10.1038/s41592-019-0459-y.

81. Haldimann, A., and Wanner, B.L. (2001). Conditional-Replication, Integration, Excision, and Retrieval Plasmid-Host Systems for Gene Structure-Function Studies of Bacteria. J. Bacteriol. *183*, 6384–6393. https://doi.org/10.1128/JB.183.21.6384-6393.2001.

82. Becker, A.H., Oh, E., Weissman, J.S., Kramer, G., and Bukau, B. (2013). Selective ribosome profiling as a tool for studying the interaction of chaperones and targeting factors with nascent polypeptide chains and ribosomes. Nat. Protoc. *8*, 2212–2239. https://doi.org/10.1038/nprot.2013.133.

83. Galmozzi, C.V., Merker, D., Friedrich, U.A., Döring, K., and Kramer, G. (2019). Selective ribosome profiling to study interactions of translating ribosomes in yeast. Nat. Protoc. *14*, 2279–2317. https://doi.org/10.1038/s41596-019-0185-z.

84. Martin, M. (2011). Cutadapt removes adapter sequences from high-throughput sequencing reads. EMBnet J. *17*, 10–12. https://doi.org/10.14806/ej.17.1.200.

85. Langmead, B., Trapnell, C., Pop, M., and Salzberg, S.L. (2009). Ultrafast and memory-efficient alignment of short DNA sequences to the human genome. Genome Biol. *10*, R25. https://doi.org/10.1186/gb-2009-10-3-r25.

STAR★METHODS

KEY RESOURCES TABLE

REAGENT or RESOURCE	SOURCE	IDENTIFIER
Antibodies		
Rabbit polyclonal anti-S2 30S ribosomal protein	Antibodies-Online	Cat#ABIN2938988; RRID:AB_3076359
Mouse monoclonal anti-polyHistidine–Peroxidase	Merck	Cat#A7058: RRID:AB_258326
HRP-conjugated goat polyclonal antirabbit	Abcam	Cat#ab205718; RRID:AB_2819160
HRP-conjugated goat polyclonal antimouse	Abcam	Cat#ab205719; RRID:AB_2755049
Bacterial and virus strains		
5-alpha Competent *E. coli*	NEB	Cat#C2987
BL21 (DE3) *E. coli*	NEB	Cat#C2527
BL21-Gold-Δlac (DE3) *E. coli*	Didovyk et al.[64]	Addgene plasmid #99247
BL21 (DE3) ΔTF *E. coli*	John Christodoulou, UCL	N/A
Chemicals, peptides, and recombinant proteins		
cOmplete, EDTA-free Protease Inhibitor Cocktail	Roche	Cat#11873580001
Puromycin dihydrochloride	Santa Cruz Biotechnology	Cat#sc-108071
Benzonase	Millipore	Cat#E1014
RNase-free DNase	QIAGEN	Cat#79254
Proteinase K	Millipore	Cat#70663
o-nitrophenyl-β-D-galactopyranoside (o-NPG)	ThermoScientific	Cat#34055
Resorufin-β-D-glucopyranoside	Merck	Cat#R4883
X-gal	Invitrogen	Cat#R0404
PureLink Genomic DNA Mini Kit	ThermoScientific	Cat#K182000
Q5 Site-Directed Mutagenesis Kit	NEB	Cat#E0554
Gibson Assembly Master Mix	NEB	Cat#E2611
Phusion High-Fidelity DNA Polymerase	NEB	Cat#M0530
RiboLock RNase Inhibitor	ThermoScientific	Cat#EO0384
Halt Protease Inhibitor Cocktail (100X)	ThermoScientific	Cat#78437
Hydroxylamine	Merck	Cat#467804
Monarch RNase A	NEB	Cat#T3018L
SuperSignal West Pico PLUS Chemiluminescent Substrate	ThermoScientific	Cat#34080
Quick Coomassie Stain	Neo Biotech	Cat#NB-45-00078
Pepsin from porcine gastric mucosa	Merck	Cat#P6887
[Glu1]-Fibrinopeptide B	Merck	Cat#F3261

EXPERIMENTAL MODEL AND STUDY PARTICIPANT DETAILS

Bacteria strains

Escherichia coli BL21(DE3), BL21-Gold-Δ*lacZ* or BL21 (DE3) Δ*tig* were cultured in ZYM 5052 autoinduction media or standard LB media with antibiotics at 37 °C or 30 °C while shaking.

METHOD DETAILS

DNA vectors

Full length and truncated *E. coli* β-galactosidase variants were expressed from a pET28 vector following an N-terminal His_6-tag TEV-protease site.[36] RNCs were expressed from pET21 plasmids encoding β-galactosidase ORFs upstream of an arrest-enhanced ribosome stalling sequence (WWWPRIRGPP).[36,61] *E. coli* DnaK and DnaJ were expressed without any tags from pET11d. *E. coli* GrpE was expressed without any tags from pET3a. Chaperone expression vectors were kind gifts from F.U. Hartl (MPI Biochemistry).

Additional mutations were introduced using site-directed mutagenesis with Q5 polymerase (NEB, E0554). All constructs used in this study were verified by sequencing and are listed in Data S3.

Expression and purification of full-length β-gal

E. coli BL21DE3 cells were transformed with a pET28 vector encoding β-gal fused to a N-terminal His_6-tag followed by a TEV protease recognition site. An overnight bacterial culture was used to inoculate Terrific broth, and the cells were grown at 37 °C to an OD of 0.8. β-gal expression was induced with 1 mM isopropyl β-D-1-thiogalactopyranoside (IPTG) and further incubation was at 16 °C for 18 h. The cells were harvested by centrifugation and resuspended in 50 mM Tris-HCl pH 7.5, 500 mM NaCl, 10 % (v/v) glycerol, 2 mM β-mercaptoethanol and 0.1 mM PMSF (Buffer A). Just before lysis, cells were supplemented with benzonase, 1 mM PMSF and lysed by two passes through a French press (Constant Systems) operating at maximum pressure of 25 kpsi and 4 °C. The clarified supernatant was loaded on to a 5 ml HisTrap HP (Cytiva) column using an AKTA pure system (Cytiva). The column washed with Buffer A, and the proteins were eluted using a linear gradient of 0–500 mM imidazole in Buffer A. Fractions with β-gal were pooled, supplemented with TEV protease, and dialyzed overnight against 20 mM Tris-HCl pH 7.5, 250 mM NaCl, 5 mM $MgCl_2$, 10 % (v/v) glycerol and 2 mM DTT at 4 °C. β-gal that was cleaved off the His tag was separated by passing the dialyzed protein through a 5 ml HisTrap HP column. The protein was concentrated, and injected into a HiPrep 26/60 Sephacryl S-300 HR column (Cytiva) equilibrated with 20 mM Tris-HCl pH 7.5, 300 mM NaCl, 10 mM $MgCl_2$, 5 % (v/v) glycerol and 3 mM DTT. Fractions containing pure protein were concentrated, flash frozen in liquid nitrogen and stored at -70 °C.

RNC buffers

RNC low-salt buffer contained 50 mM HEPES-NaOH pH 7.5, 12 mM $Mg(OAc)_2$, 100 mM KOAc, 1 mM DTT and 8 U/mL RiboLock RNase inhibitor (ThermoScientific, EO0384). RNC high-salt sucrose cushion contained 35% sucrose, 50 mM HEPES-NaOH pH 7.5, 12 mM $Mg(OAc)_2$, 1 M KOAc, 1 mM DTT, 8 U/mL RiboLock RNase inhibitor and 0.2x Halt Protease Inhibitor Cocktail (ThermoScientific, 78437). RNC low-salt sucrose cushion contained 35% sucrose, 50 mM HEPES-NaOH pH 7.5, 12 mM $Mg(OAc)_2$, 100 mM KOAc, 1 mM DTT, 8 U/mL RiboLock RNase inhibitor and 0.2x Halt Protease Inhibitor Cocktail.

Expression and purification of ribosome:nascent chain complexes (RNCs)

RNCs were expressed and purified as described previously[36] with slight modifications. NCs contain an N-terminal muGFP for affinity purification, which is later cleaved. In short, BL21(DE3) *E. coli* cells were transformed with plasmids encoding RNC constructs and grown in ZYM-5052 autoinduction media[62] for 18 h at 37 °C. As indicated, expression cells were either TF knock-out cells (*Δtig*, John Christodoulou, UCL) or β-gal knock-out cells (*ΔlacZ*, Addgene, 99247[63]). Cells were pelleted (4,000 g, 30 min) and resuspended in RNC lysis buffer (70 mM Tris, pH 7.5, 150 mM KCl, 10 mM $MgCl_2$, 8 U/mL RiboLock RNase inhibitor, 0.5x Halt Protease Inhibitor Cocktail, 2 mg/mL lysozyme, 0.05 Kunitz units/μL RNase-free DNase (QIAGEN, 79254)). Following an incubation (30 min, 4 °C) and subjecting resuspended pellets to at least 2 freeze-thaw cycles at -80 °C, the soluble fraction was separated by centrifugation (20 min, 16,000 g) and centrifuged (2 h, 264,000 g) through RNC high-salt sucrose cushion to isolate ribosomes in the pellet. The pellet was resuspended in RNC low-salt buffer and applied to in-house prepared GFP-clamp-agarose beads[64] for 16 hours at 4 °C. RNCs were selectively eluted by muGFP-tag cleavage with HRV 3C protease, and further purified by pelleting through a second sucrose cushion (2 h, 264,000 g). Pellets were resuspended in RNC low-salt buffer, snap-frozen in liquid nitrogen and stored at −80 °C. Sequences of all purified RNCs are listed in Data S3.

Expression and purification of β-galactosidase truncations

Expression and purification of β-galactosidase truncations was performed as described previously[36] with slight modifications. BL21(DE3) *E. coli ΔlacZ* cells (Addgene, 99247[63]) transformed with plasmid encoding C-terminally truncated β-gal 1-440, 1-519, 1-725 or β-gal domain 5 (D5, 739-1023) were grown in LB at 37 °C until OD_{600} 0.6–0.8 and protein expression was subsequently induced with 1 mM IPTG for an additional 18 hours at 16-18 °C. BL21(DE3) *E. coli ΔlacZ* cells transformed with plasmid encoding C-terminally truncated β-gal 1-490 were grown in ZYM-5052 autoinduction media[62] for 18 h at 37 °C. Cells were harvested (4,000 g, 30 min), resuspended in Buffer A (50 mM Tris-HCl, pH 7.5, 500 mM NaCl, 10% glycerol, 2 mM β-mercaptoethanol, 100 mM PMSF) supplemented with 1 mg/mL lysozyme, benzonase (Millipore, E1014) and Complete EDTA-free protease inhibitor cocktail (Roche, 11873580001), and lysed by sonication. Lysate was clarified by centrifugation (60,000 g, 45 min) and then applied to HisTrap HP column (Cytiva, 17524802) equilibrated in Buffer A. Peak fractions from gradient elution with 500 mM Imidazole were treated with TEV protease (48 h, 4 °C) and dialysed against Buffer A. Uncleaved protein was removed using a HisTrap HP column equilibrated in Buffer A. The flow-through was further purified using a Superdex 200i 10/300 (Cytiva, 28990944) equilibrated in Buffer B (20 mM Tris-HCl, pH 7.5, 300 mM NaCl, 10 mM $MgCl_2$, 3 mM DTT, 5% glycerol), and pure protein was concentrated and snap-frozen in liquid nitrogen for storage at −80 °C. Sequences of purified proteins are listed in Data S3.

Expression and purification of DnaK, DnaJ and GrpE

DnaK, DnaJ and GrpE were expressed and purified as described previously[36] without any modifications. BL21(DE3) E. coli transformed with DnaK-, DnaJ- or GrpE-encoding plasmids were grown in LB at 37 °C until OD600 0.6–0.8 and subsequently induced for expression with 0.5 mM IPTG for an additional 5 hours at 30 °C.

DnaK-expressing cells were harvested by centrifugation (4,000 g, 30 min), resuspended in lysis buffer (20 mM Tris-HCl, pH 7.4, 1 mM EDTA, 1 mg/mL lysozyme, 0.2 mM PMSF, benzonase, and Complete EDTA-free protease inhibitor cocktail) and lysed by sonication. Clarified lysate (60,000 g, 45 min) was applied onto RESOURCE Q column (Cytiva) preequilibrated in Buffer Q (20 mM Tris-HCl, pH 7.4, 1 mM EDTA). Peak fractions eluted with NaCl were combined and desalted on HiPrep 26/10 desalting column (Cytiva) equilibrated in Buffer H (20 mM HEPES-NaOH, pH 7.4, 5 mM Mg(OAc)2) and loaded onto a HiTrap Heparin column (Cytiva) equilibrated in Buffer H. Peak fractions eluted with an NaCl gradient were exchanged into Buffer Q and loaded onto a RESOURCE Q column. DnaK-containing fractions from NaCl elution were combined and loaded onto a Superdex 200i 10/300 column in 20 mM HEPES-NaOH, pH 7.4, 5 mM Mg(OAc)2, 100 mM NaCl, 5% glycerol, 1 mM DTT. Pure DnaK was concentrated, snap-frozen in liquid nitrogen and stored at −80 °C.

DnaJ-expressing cells were harvested by centrifugation (4,000 g, 30 min), resuspended in lysis buffer (50 mM Tris-HCl, pH 8.5, 10% sucrose, 10 mM DTT, 10 mM EDTA, 0.6% Brij58, 1 mg/mL lysozyme, benzonase, and Complete EDTA-free protease inhibitor cocktail) and lysed by sonication. The lysate was centrifuged (60,000 g, 45 min) and the pellet was resuspended in Buffer U (2 M urea, 50 mM Tris-HCl, pH 8.5, 5 mM DTT, 10% sucrose, 0.1% Triton-X). Resolubilised protein was separated from aggregated material in the pellet by centrifugation (60,000 g, 45 min), and the supernatant was loaded onto RESOURCE Q column in Buffer U. Peak fractions eluted with Buffer Q2 (50 mM Tris-HCl, pH 8.5, 5 mM DTT, 10% glycerol, 0.05% Brij58, 1 M NaCl) were combined and desalted using a HiPrep 26/10 desalting column equilibrated in Buffer S (20 mM sodium phosphate, pH 6.8, 5 mM DTT, 10% glycerol, 0.05% Brij58, 100 mM KCl). Protein was subsequently loaded onto RESOURCE S column (Cytiva) preequilibrated in Buffer S. Protein eluted with KCl was exchanged into Buffer S, loaded onto a HiTrap Heparin column, and eluted with a KCl gradient. DnaJ-containing fractions were combined and loaded onto Superdex 200i 10/300 column in 25 mM Tris-HCl, pH 7.5, 10% glycerol, 5 mM DTT, 100 mM KCl. Pure DnaJ was concentrated and snap-frozen in liquid nitrogen for storage at −80 °C.

GrpE-expressing cells were harvested, lysed and the lysate was clarified as for DnaK-expressing cells. Ammonium sulfate was added to a final concentration of 0.35 $g.L^{-1}$ and the solution was stirred for 20 min. The pellet was harvested by centrifugation (60,000 g, 45 min), resuspended in Buffer Q and loaded onto a RESOURCE Q column. The protein was eluted using an NaCl gradient (0 - 1 M) and fractions containing GrpE were loaded onto a Superdex 200i 10/300 column in Buffer E (25 mM HEPES-NaOH pH 8.0, 1 mM EDTA, 10 mM BME, 20% glycerol). Fractions containing pure DnaK were concentrated, snap-frozen in liquid nitrogen and stored at −80 °C. Sequences of purified proteins are listed in Data S3.

Size-exclusion chromatography with multi-angle light scattering

100 μL of pure protein was applied at 0.5 mL/min to Superose 6i 10/300 GL column (Cytiva) equilibrated in 30 mM Tris-HCl, pH 7.5, 10 mM $MgCl_2$, 300 mM NaCl, 2 mM DTT for an isocratic elution in the same buffer. The concentrations of injected proteins are indicated in figure legends and were determined using absorbance at 280 nm and the Expasy ProtParam predicted extinction coefficients.[65] UV absorbance, light scattering (LS) and differential refractive index (dRI) were monitored throughout elution. The molecular mass of the eluate was determined from LS and dRI data using the ASTRA software.

Immunoblotting

Following SDS-PAGE, proteins were transferred onto a PVDF membrane using a Trans-Blot Turbo Transfer System (BioRad). Membranes were blocked in PBS-Tween with 5% non-fat milk for 1 hour at RT and incubated with appropriate primary antibodies (1:1,000 dilution in PBS-Tween with 5% non-fat milk) for 1 hour at RT. Following three washes (5 min, RT) with PBS-Tween, membranes were incubated with appropriate HRP-conjugated secondary antibodies (1:10,000 dilution in PBS-Tween with 5% non-fat milk) for 1 hour at RT and washed. Membranes were developed by enhanced chemiluminescence using SuperSignal West Pico PLUS Chemiluminescent Substrate (ThermoScientific, 34080). Primary antibodies used for each immunoblot are specified in figure legends – these include monoclonal mouse anti-β-galactosidase antibody (Santa Cruz Biotechnology, antibody sc-65670, 1:1000) and polyclonal chicken anti-β-galactosidase N-terminus antibody (abcam, ab106567, 1:1000). These were detected with corresponding HRP-conjugated secondary antibodies – either goat polyclonal anti-mouse (abcam, ab205719) or anti-chicken (abcam, ab97135). Quantification of band-specific chemiluminescent signal was performed in Fiji[66] by measuring the area under a signal peak corresponding to the given band.

β-galactosidase refolding

β-gal refolding experiments were performed essentially as described previously.[33] The concentration of β-gal was estimated using the Bradfords assay reagent (Bio-Rad) with Bovine Serum Albumin Standard (ThermoFisher). The unfolding reaction containing 10 μM β-gal in 100 mM sodium phosphate pH 7.5, 8 M urea, 1 mM EDTA and 10 mM DTT was incubated overnight at 10 °C. For the native control, β-gal was incubated in the same buffer without urea. Refolding reactions were initiated by diluting the unfolding reaction (or native control) 10-fold into the refolding buffer containing 100 mM sodium phosphate pH 7.5, 0.7 M urea, 1 mM $MgCl_2$ and 5 mM DTT at 10 °C. To measure the extent of refolding, 1 μl of the refolding reaction was added to 300 μl of reaction mix containing 30 mM TES pH 7.0, 145 mM NaCl, 10 mM $MgSO_4$, 0.1 mM EDTA and 2 mM o-nitrophenyl-β-D-galactopyranoside. The increase in absorbance at 420 nm was measured using Spectramax Plus 384 plate reader (Molecular Devices) operating at 23 °C and the slope of the progress curve was recorded. For refolding in presence of Hsp70 system, the refolding as well as the native control reaction contained 100 mM Hepes-sodium pH 7.5, 10 mM $MgCl_2$, 100 mM KCl, 5 mM DTT, 3 μM DnaK, 1 μM DnaJ, 1.5 μM GrpE and 2.5 mM

ATP. Refolding yield (ratio of activity of refolded β-gal to the activity of the native control) was plotted against time in Prism (GraphPad Software), and the data were fit to a one-phase association model to determine the half-time and rate constant of refolding.

β-galactosidase RNC activity assay

Enzymatic activity of β-gal-containing IVTs, β-gal RNCs and β-gal C-terminal truncations was measured in RNC low-salt buffer with final 2.1 mM o-nitrophenyl-β-D-galactopyranoside (oNPG) by following absorbance at 420 nm at 25 °C and recording the slope of the progress curve. See figure legends for experiment-specific information about final protein concentrations. Unless otherwise stated, reactions were diluted 200-fold in oNPG-containing buffer just prior to activity measurement.

In vitro translation

IVT reactions were performed using the PURExpress *in vitro* Protein Synthesis Kit (NEB, E6800S). Solutions A and B were pre-mixed according to manufacturer's instructions at 2:1.5 ratio on ice, and all reactions were supplemented with RNasin Ribonuclease Inhibitor (Promega, N2111) at a final concentration of 2 units/μL. Any supplemented plasmid DNA was added at final 10 μg/μL concentration. For continuous IVT monitoring, fluorogenic resorufin-β-D-glucopyranoside (Merck, R4883, λ_{ex} 570 nm, λ_{em} 585 nm) was added at final 250 μM. Unless otherwise stated, expression was subsequently conducted at 37 °C for up to 2 hours. Expressed IVT samples were then analysed for β-galactosidase activity, β-galactosidase amounts or used as an input for a sucrose cushion centrifugation (264,000 g, 2 hours, 4 °C) through a RNC low-salt sucrose cushion. For comparison to the activity of in vivo and IVT-produced β-galactosidase (Figure 1C), purified enzyme was titrated into an IVT mixture in the absence of plasmid DNA.

Light scattering

Scattering was measured at 320 nm using a UV/visible spectrophotometer (V-760, Jasco) equipped with a temperature-controlled cuvette chamber. The unfolding reactions contained 10 μM β-gal (or 50 μM), 8 M urea, 100 mM sodium phosphate pH 7.5, 1 mM EDTA and 10 mM DTT. The unfolding reactions were diluted 10-fold into buffer containing 100 mM sodium phosphate pH 7.5, 1 mM $MgCl_2$, 5 mM DTT, and either 0.7 or 0 M urea. The reactions were mixed and transferred to a cuvette held at 10 or 25 °C.

Native PAGE

30 μl of refolded or native control reactions containing 1 μM β-gal were mixed with 10 μl of 4X native loading buffer containing 0.4 M Tris-HCl pH 8.0, 40 % (v/v) glycerol, 0.01 % (w/v) bromophenol blue, and snap frozen in liquid nitrogen. The samples were thawed and loaded immediately into cold 7% NuPage Tris-Acetate gels (ThermoFisher). The gel tank and the running buffer (24 mM Tris base, 191 mM glycine) were cooled for several hours in the cold room before loading the samples. For activity staining, the gels were incubated in a solution containing 50 mM Tris-HCl pH 7.0, 150 mM NaCl, 10 mM $MgCl_2$ and 0.1 mg ml^{-1} X-gal, at 23 °C. For western blotting, the gel was incubated with 1x PBST for 5 min and the proteins were blotted to a PVDF membrane using the Trans-Blot Turbo system (Bio-Rad). The membrane was blocked using 5 % (w/v) skimmed milk power in PBST and incubated with the β-gal antibody (SC-65670, Santa Cruz Biotechnology) overnight at 4 °C. The membrane was washed and incubated with anti-mouse HRP secondary antibody (ab205719, Abcam) and developed using SuperSignal West Pico PLUS chemiluminescent substrate (ThermoFisher). Imaging was done using Amersham ImageQuant 800 (Cytiva). The gels were stained using Quick Coomassie Stain (Neo-Biotech).

Limited proteolysis

RNCs were diluted to 0.5 μM in RNC low-salt buffer and cooled to 4 °C. Subsequently a reference aliquot was removed before proteolysis was initiated by addition of Proteinase K to a final concentration of 2.5 ng/μL. Aliquots of the proteolysis reactions were removed and quenched at different times by 1:1 mixing with 5 mM PMSF in RNC low-salt buffer. Quenched sample were then resolved by SDS-PAGE.

Negative stain EM

Full-length β-gal or β-gal truncation 1-725 purified from Δ*lacZ* cells were diluted to 1 μM in RNC low-salt buffer. 4 μL were applied to copper grids (EM Resolutions, C300Cu100) coated with a continuous carbon only support films (15-20 nm) that had been glow discharged (25 mA, 60s) in a GloQube Plus Glow Discharge System (Quorum Technologies). After 1-2 minutes of incubation, excess sample was removed with filter paper (Whatman, 1001-090). Next, 40 μL of 2% uranyl acetate was applied three times for 20 s. Excess stain was removed with filter paper after each application and finally grids were air-dried. Micrographs were collected on a FEI Tecnai 12 Spirit 120 kV TEM with magnification 67,000x in a low-dose mode.

Cryo-EM sample preparation

4 μl of purified $RNC_{1\text{-}510}$, prepared as described above (50 mM HEPES pH 7.5, 12 mM MgOAc2, 100 mM KOAc, 1 mM DTT, RiboLock RNase inhibitor and 0.1% octyl glucoside), was deposited on 45 nm gold film 1.2/1.3 hole pattern 300 mesh grids (au-flat™, EMS) glow-discharged in air for 60 s at 40 mA in an Emitech K100X glow discharge unit to render them hydrophilic, then blotted for 6 seconds using a Vitrobot Mark IV (FEI/Thermo Fisher Scientific) at 4 °C and 100% humidity and flash frozen in liquid ethane.

Cryo-EM data collection and single particle analysis

In total, 9,384 micrographs were collected using Titan Krios cryo-EM (Thermo Fisher Scientific) operated at 300 kV, equipped with a Falcon4i detector. Images were collected using EPU software (Thermo Fisher Scientific) with a total of 1935 EER frames and nominal magnification of 75,000× (1.08 Å per pixel). The electron dose was 29.8 electrons per $Å^2$ with dose per frame being 1.192 electrons per $Å^2$. The defocus range was −1.3 to −2.8 μm. Beam-induced motion correction and per-frame radiation damage weighting with 5 by 5 patches were performed using MotionCor2 algorithms implemented in RELION.[67] CTF estimation was done on motion corrected micrographs with CTFFIND-4.1.[68] Micrographs with estimated resolution of 9 Å or higher were retained, resulting in 58 discarded micrographs. Initial particle picking was done using TOPAZ,[69] on a smaller micrograph subset (348 micrographs) with particle diameter of 280. 25,827 particles were selected and used to train a TOPAZ picking model. Using the full dataset, 4,974,533 particles were picked. Particle coordinates were extracted using a square box size of 320 pixels with 2-fold binning. Extracted particles were subjected to two rounds of 2D classification in RELION, with the first round ignoring CTFs until first peak. 835,178 particles were selected for a consensus 3D refinement, using an *ab-initio* map from CryoSPARC4.6[70] as a reference. From the resulting consensus refinement at 4.37 Å resolution, a solvent mask was created and used for 3D classification without alignment. Here, there were 3 classes, one with 50S-only particles (240,640 particles, 28.8%), one with poor resolution 70S (109,325 particles, 13.1%) and the largest class containing well-aligned 70S particles (485,213 particles, 58.1%). The latter class was further classified based on tRNA site occupancy. The particles were imported into CryoSPARC, where utilising an 80 Å spherical mask and 3D variability analyses,[71] 3 clusters of particles were identified. Classes containing both the A- and P- site tRNA were pooled together to a total of 389,472 particles (80.2%). These particles were then refined in CryoSPARC via Non-Uniform Refinement[72] and transferred back to RELION via pyem0.65. The particles were re-extracted without binning and subjected to 3D refinement in RELION followed by iterative rounds of CTF refinement where anisotropic magnification, 4th order aberrations and trefoil were estimated and followed by per-particle defocus and per-micrograph astigmatism fitting. Particles were then subjected to per-particle motion correction by Bayesian polishing. A final refinement resulted in a 2.86 Å-resolution reconstruction. The map was then sharpened using a B-factor of 61.45 during post-processing in RELION, as shown in Figure S9, otherwise the unsharpened map has been used. Associated figures were created using UCSF ChimeraX version1.9.[73]

Model building and real-space refinement

Empty ribosome structures (PDB: 7K00[38]; 8QOA[37]) were used as initial models for atomic model building. These models were rigid-body fitted into map using UCSF ChimeraX. Then, each chain was real-space-refined in ISOLDE.[74] The nascent chain was built *de novo* based on $RNC_{1\text{-}510}$ sequence, first fitting residues of the amphipathic helix $_{466}$ANHDALYRWIKSV$_{478}$ and stalling sequence WWWPRIRGP as these had the best-defined side-chains. The atomic models were subjected to multiple rounds of real-space refinement in Phenix version 1.21.2[75] and ISOLDE was used to manually fix all outliers and bad geometries. Validation of the models was carried out using Phenix, wwwPDB Validation, and the Molprobity server[76] (http://molprobity.biochem.duke.edu/).

Circular dichroism spectroscopy

Peptide Ac-ANHDALYRWIKSV-NH_2 synthesized in-house was resuspended in water and diluted to 0.15 mg/mL in 20 mM sodium phosphate buffer, pH 7 prior to circular dichroism measurement at 20 °C. The average of 25 scans (range = 190 to 260 nm, bandwidth = 2 nm, increment = 0.2 nm) was recorded and corrected using a buffer blank. The data were subsequently deconvoluted to estimate the relative secondary structure content using ContinLL, SELCON3, and CDSSTR methods.[61–64,75,77] The average value obtained from the three deconvolution methods was reported.

Quantification and statistical analysis

Band intensities on immunoblots and SDS-PAGE gels were quantified in Fiji.[66] All statistical analyses and curve fitting were performed in GraphPad Prism 10. Hydrophobicity values of solved protein structures were calculated using ChimeraX Molecular Lipophilicity Potential. Hydrophobic clusters composed of Ile, Leu and Val were identified using the ProteinTools server[78] (https://proteintools.uni-bayreuth.de/). The residues constituting the long and activating interface were identified using the PDBePISA server.[79]

Pulse-labelled HDX-MS analysis of β-gal refolding

The refolding reaction was set-up as described above. At different times, reactions were exchanged into the deuteration buffer using spin desalting columns (Micro Bio-Spin 6, Bio-Rad). The columns were equilibrated four times with 500 μl of deuteration buffer composed of 10 mM sodium phosphate (pH_{read} = 7.01 at 23 °C), 1 mM $MgCl_2$, 5 mM DTT, 1.5 M urea (99.9% D2O). The deuteration buffer was prepared by mixing the stock solutions of the components which were prepared in D_2O and the final pH_{read} was 7.48 at 23 °C. Undeuterated control reaction was exchanged into a solution prepared with water but identical in composition to deuteration buffer. 50 μl of the refolding reaction was pipetted into the spin columns and spun at 1000 ×g for 1 min at 23 °C. The exchange was immediately quenched by mixing 45 μl of the deuteration reaction with 15 μl of quench buffer (1 M orthophosphoric acid with pH adjusted to 2.12 using NaOH), and the tube was flash frozen in liquid nitrogen and stored at -70 °C. Triplicate independent refolding reactions were performed and these results are reported in the manuscript. The experimental outcome was validated by performing a biological replicate experiment using an independent protein purification where fewer time points of refolding were sampled.

The samples were thawed and 50 μl was immediately injected into an Acquity UPLC M-class system (Waters) equipped with an HDX manager. The injection order was randomized. The protein was pumped at 200 μL min^{-1} for 2 min over an Enzymate BEH pepsin column (5 μm, 2.1 mm x 30 mm, Waters) held at 20 °C. The peptides were trapped and desalted on an Acquity UPLC BEH C18 Van-guard trap column (1.7 μm, 2.1 mm x 5 mm, Waters) held at 0 °C. The peptides were eluted at 40 μl min^{-1} and separated on an Acquity UPLC BEH C18 column (1.7 μm, 100 mm x 1 mm, Waters) held at 0 °C, using a 3-35% gradient of acetonitrile in 0.1 % (v/v) formic acid over 16 min. The peptides were detected using a SYNAPT G2-Si $HDMS^E$ instrument in ion mobility mode, acquiring in positive ion mode over a range of 50 to 2,000 m/z. The electrospray ionization source temperature was 80°C and the spray voltage was 3.0 kV. The lock mass calibration was performed using [Glu^1]-Fibrinopeptide B (50 fmol/μL, Merck, F3261).

To prepare the maximally deuterated control, 1 μM β-gal in 0.1 % formic acid was digested for 5 min at 25 °C using pepsin beads. The beads were separated using a spin filter, and 45 μl of the digest was dried in a speed vac. The peptides were resuspended in 45 μl of D_2O and incubated for 18 h at 35 °C. This was then mixed with 15 μl of the quench buffer and injected immediately into the mass spectrometer as described above.

The peptides in undeuterated β-gal were searched using Protein Lynx Global Server (version 3.0.3, Waters) search engine. In the workflow parameters, a database consisting of β-gal sequence, non-specific cleavage and oxidation of methionine as variable modification were specified. A low energy threshold of 135 counts and elevated energy threshold of 30 counts were specified in the processing parameters. The peptides identified by Protein Lynx Global Server were input into DynamX (version 3.0.0, Waters) and filtered using the settings minimum products per amino acid of 0.2 and minimum consecutive products of 2. The spectra were manually inspected to rectify incorrect peak assignments and peptides with poor quality spectra were rejected.

DynamX analysis was exported as a cluster file. The mass of the peptide was calculated using the formula PepMass = Z × (Center – Proton Mass). Relative deuterium uptake of a peptide was calculated by subtracting the average mass of triplicate values for the undeuterated peptide from the mass of the deuterated peptide. For each peptide, the relative uptake of refolded sample (29 h of refolding) was subtracted from unfolded sample (0.06 h, first time point sampled for the refolded protein). Peptides experiencing an overall change in mass less than 0.5 Da were given a half-life of 0 min. These were typically located in exposed loops which do not change in deuterium uptake during refolding. For the remaining peptides, data describing relative uptake versus time were exported into Graphpad Prism, and fit to one-phase decay equation to generate folding half-times. Per-residue half-time was calculated by averaging the values from overlapping peptides. All plotted uptake data and a summary of experimental conditions[80] are shown in Data S1. The MS data have been deposited to the ProteomeXchange Consortium via the PRIDE partner repository with the dataset identifier PRIDE: PXD063232.[60]

Equilibrium HDX-MS analysis of RNCs and β-gal truncations

HDX-MS was conducted as described previously[36] with some modifications. In short, stock samples were prepared in RNC low-salt buffer at final 5-6 μM for RNCs and empty ribosomes (NEB, P0763S), and at final 15-20 μM for C-terminally truncated or full-length β-galactosidase. Deuterium labelling was initiated by mixing 3 μL of stock samples with 27 μL deuteration buffer (10 mM HEPES-NaOH, pH 7.1, 30 mM KOAc, 12 mM $Mg(OAc)_2$, 1 mM DTT, RiboLock RNase inhibitor (ThermoScientific), 97% D_2O) at 25 °C. After labelling at 25 °C for 10 or 100 seconds, the reaction was quenched with an equal volume (30 μL) of ice-cold quench buffer (100 mM sodium phosphate, pH 1.4, 4 M guanidium hydrochloride, 10 mM TCEP). The pH after quenching was 2.5. Digestion was initiated by addition of 20 μL pepsin-agarose 50% v/v bead slurry (prepared in-house as described previously[36]) equilibrated in 0.1% formic acid. Following 100 s of digestion at 10 °C with rapid mixing every 30 seconds, the sample was centrifuged (13,000 g, 15 s, 0 °C) through 0.22 μm PVDF filters (Millipore, UFC30GVNB). The flow through was immediately snap-frozen in liquid nitrogen for short-term storage. The same protocol was followed to prepare undeuterated controls, except the deuteration buffer was replaced by a H-based buffer (10 mM HEPES-NaOH in H_2O, pH 7.5, 30 mM KOAc, 12 mM $Mg(OAc)_2$, 1 mM DTT, RiboLock RNase inhibitor).

Frozen samples were rapidly thawed and immediately injected into an Acquity UPLC M-class system with the cooling chamber containing the chromatographic columns kept at 0 ± 0.2 °C throughout data collection. Peptic peptides were trapped and desalted for 4 minutes (200 μL/min) on a 2.1 mm X 5 mm, C4 trap column (Acquity BEH C4 Van-guard pre-column, 1.7 μm, Waters, 186004623) then separated on a reverse phase Acquity UPLC HSS T3 column (1.8 μm, 1 mm X 50 mm, Waters, 186003535) at a flow rate of 90 μL/min. Peptides were eluted over 25 minutes using a 3-30% gradient of acetonitrile in 0.1% formic acid. Analysis was performed using a Waters Synapt G2Si $HDMS^E$ instrument in ion mobility mode, acquiring in positive ion mode over a range of 50 to 2,000 m/z with the conventional electrospray ionisation source. Calibration of the mass spectrometer was achieved using [Glu^1]-Fibrinopeptide B (50 fmol/μL, Merck, F3261) and the instrument was operated at a source temperature of 80 °C with the capillary set to 3 kV.

MS^E data were processed using Protein Lynx Global Server (PLGS, Waters) to identify peptides in the undeuterated control samples using information from a non-specific cleavage of a database containing sequences of *E. coli* β-galactosidase, Trigger Factor, 70S ribosomal proteins as well as porcine pepsin. PLGS search was performed using energy thresholds of low = 135 counts and elevated = 30 counts. Peptides identified by PLGS were subsequently filtered and processed in DynamX (Waters) with filters of minimum products per amino acid of 0.05 and minimum consecutive products of 1. All spectra were manually inspected, and poor-quality assignments were removed. Any peptides assigned to nascent chains that were also detected in empty ribosome control samples were removed. Additionally, peptides assigned to β-galactosidase in nascent chains but not in isolated β-galactosidase, were also removed. Relative deuterium uptake in Da was calculated by subtracting the centroid mass of undeuterated peptides from those of deuterated peptides. Determined mean values of deuterium uptake are relative as they are not corrected for back-exchange. All

HDX-MS experiments were performed in technical triplicates for each sample at each deuteration time and used to calculate the reported mean. In some cases, we also performed biological replicates using independent purifications. All plotted uptake data, peptide coverage maps, and a summary of experimental conditions[80] are shown in Data S2. The MS data have been deposited to the ProteomeXchange Consortium via the PRIDE partner repository with the dataset identifier PRIDE: PXD060082.[60]

Selective ribosome profiling (SeRP)

lacZ-mEYFP under the control of the IPTG inducible tac promoter was integrated in the *E. coli* MC4100 genome at the λ-phage attachment site.[81] Exponentially growing cells were harvested at OD600 = 0.45 – 0.5 by rapid-filtration and flash-freezing in liquid nitrogen. Expression of lacZ-mEYFP was induced by 10 μM IPTG (f.c.) for 15 min before cell harvest. Cell pellets were lysed under cryogenic conditions by mixer milling (2 min, 30 Hz) with SeRP lysis buffer (50 mM HEPES KOH pH 7.0, 100 mM NaCl, 10 mM MgCl2, 5 mM CaCl2, 50 μg/ml chloramphenicol, 1 mM PMSF, cOmplete EDTA-free protease inhibitor (Roche)). Upon thawing on ice, RP lysis buffer containing DNaseI was added to the lysate and the lysate was cleared by centrifugation (20 000 xg, 10 min, 4 °C). The supernatant was digested with self-made micrococcal nuclease (MNaseI) for 1 h at 25 °C, quenched by EGTA (f.c. 6 mM). For the total translatome, ribosomes from one-fifth of the lysate were purified by sucrose density centrifugation (20 mM Tris-HCl pH 8.0, 100 mM NH4Cl, 10 mM MgCl2, 50 μg/ml chloramphenicol) and ribosome-protected mRNA-footprints were isolated by acid phenol extraction as previously described.[82] For the selected translatome, the remaining lysate was incubated with GFP-binder coupled sepharose beads (800 μl 1:1 suspension) for 1 h at 4 °C by end-to-end rotation. Beads were washed three times with wash buffer (50 mM HEPES KOH pH 7.0, 100 mM NaCl, 10 mM MgCl2, 50 μg/ml chloramphenicol, 1 mM PMSF, cOmplete EDTA-free protease inhibitor (Roche), 0.02% (v/v) Tween-20) for 5 min at 4 °C. Ribosome protected footprints were extracted by acid phenol extraction. cDNA libraries for deep sequencing analysis were generated as described previously[82] and sequenced on a HiSeq 2000 v4 (Illumina).

Disome Selective Profiling (DiSP)

E. coli MG1655 cells were grown at 37 °C in EZ RDM with lactose as the sole carbon source and harvested by rapid filtration and flash-freezing in liquid nitrogen at OD600 = 0.45 – 0.5. Cells were lysed in the presence of DiSP lysis buffer (50 mM HEPES KOH pH 7.0, 100 mM NaCl, 10 mM $MgCl_2$, 5 mM $CaCl_2$, 50 μg/ml chloramphenicol, 1 mM PMSF, cOmplete EDTA-free protease inhibitor (Roche), 0.4% (v/v) Triton X-100, 0.1% Nonidet P40 Substitute) under cryogenic conditions by mixer milling (2 min, 30 Hz). Upon thawing 750 uL DiSP lysis buffer containing DNase I was added and the lysate was cleared by centrifugation (20 000 xg, 10 min, 4 °C). The supernatant was digested with self-made micrococcal nuclease for 10 min at 25 °C, quenched by EGTA (f.c. 6 mM). 250 μg total RNA was layered over a 5%–45% sucrose gradient (50 mM HEPES-KOH pH 7.0, 500 mM KCl, 10 mM $MgCl_2$, 50 μg/mL chloramphenicol) and separated by ultracentrifugation for 3.5 h at 35.000 rpm, 4 °C. Monosome and disome fractions were isolated and the RNA extracted by acid phenol. cDNA libraries for deep sequencing analysis were generated as described previously[83] and sequenced on a NextSeq 550 (Illumina).

Ribosome profiling data analysis

LacZ-SeRP libraries were sequenced on a HiSeq 2000 (Illumina). 3′ adapter sequences were trimmed from demultiplexed raw sequencing files using Cutadapt[84] with the following parameters: -q20 -m23 –discard-untrimmed -O6 -a CTGTAGGCACCATCAATTCGTATGCCGTCTTCTGCTTG. Trimmed reads were aligned to the E. coli reference genome (NC_000913.3) using Bowtie1[85] with the parameters -m1 -t -n2 –best –strata. Aligned reads were assigned to the P-site using a custom Julia script (Script2) published previously[20] with the parameters –length 15:45 –assignment_type 3.

DiSP libraries were sequenced on a NextSeq 550 (Illumina). 3′ adapter sequences were trimmed from demultiplexed raw sequencing files using Cutadapt with the parameters -q 20 -m23 –discard-untrimmed -O6 -a ATCGTAGATCGGAAGAGCACACGTCTGAACTCCAGTCAC. Unique molecular identifiers (UMI) were extracted from each read and added to the read identifier using a custom Julia script (Script1) published previously[20] with the parameters –umi3 5 –umi5 2.

Trimmed reads were aligned to the E. coli reference genome (NC_000913.3) using Bowtie1 with the parameters -m 1 -t -n 2 –best –strata. Aligned reads were deduplicated based on their UMI and assigned to the P-site using Script2 with the parameters –use_umis –length 15:45 –assignment_type 3.